Abstract We review recent theoretical and experimental efforts toward developing an all-optical switch based on transverse optical patterns. Transverse optical patterns are formed when counterpropagating laser beams interact with a nonlinear medium. A perturbation, in the form of a weak switch beam injected into the nonlinear medium, controls the orientation of the generated patterns. Each state of the pattern orientation is associated with a state of the switch. That is, information is stored in the orientation state. A realization of this switch using a warm rubidium vapor shows that it can be actuated by as few as 600 ± 40 photons with a response time of 5 μs. Models of nonlinear optical interactions in semiconductor quantum wells and microresonators suggest these systems are also suitable for use as fast all-optical switches using this same conceptual design, albeit at higher switching powers.

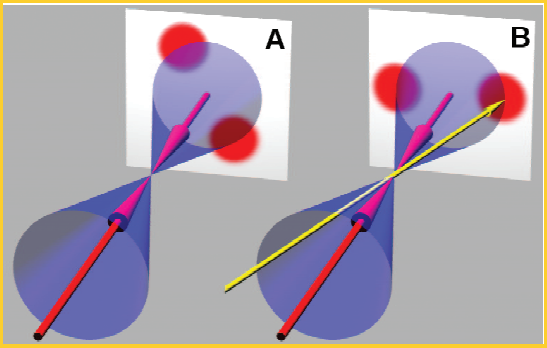

A pair of counterpropagating beams induce an instability that generates transverse optical patterns. (A) Two spots form the unperturbed far-field pattern. (B) A weak beam incident at an angle to the pump beam axis causes the generated pattern to rotate. From Ref. [1]

Transverse optical patterns for ultra-low-light-level all-optical switching

Andrew M. C. Dawes, [1,*] *Daniel J. Gauthier,* [2] *Stefan Schumacher,* [3,4] *N.H. Kwong,* [3] *R. Binder* [3] *and Arthur L. Smirl* [5]

[1] Department of Physics, Pacific University, Forest Grove, OR 97116, USA
[2] Department of Physics, Fitzpatrick Institute for Photonics, and Center for Nonlinear and Complex Systems, Duke University, Durham, NC 27708, USA
[3] College of Optical Sciences, University of Arizona, Tucson, Arizona 85721, USA
[4] Physics Department, School of Engineering and Physical Sciences, Heriot-Watt University - Edinburgh, EH14 4AS, UK
[5] Laboratory for Photonics and Quantum Electronics, 138 IATL, University of Iowa, Iowa City, Iowa 52242, USA

Received: ...
Published online: ...

Key words: all-optical, switching, nonlinear, transverse, counterpropagating

1. Introduction

In the past decade, the rapid bandwidth increase in communication networks has been enabled by advances in opto-electronic technology. However, bandwidth improvements cannot continue indefinitely as opto-electronic devices face thermal dissipation limits that are fundamental to processing information in the electronic domain [2]. Photonics offers a wide range of novel information processing technologies with the potential for much greater bandwidth. In particular, devices that process information in the optical domain can operate on parallel channels, with high bandwidth, and with markedly higher information density.

To process information all-optically, beams of light must interact with one another, which can only occur in nonlinear media. Optical nonlinearities are typically weak, requiring high intensities in order to generate significant effects. A current goal in the field of nonlinear optics is to reduce the power required for nonlinear interactions. One application of nonlinear optics is the development of efficient telecommunications devices where strong non-

e-mail: dawes@pacificu.edu

linearities reduce device power requirements. In addition, there is a need to operate devices at the ultimate, single-photon level. Few-photon or ultra-low-light nonlinear optics has many potential applications in quantum information science [3]. Several recent experiments in the photonics field have demonstrated ultra-low-light nonlinear optical effects using various techniques including high-finesse cavities [4, 5], plasmonic nanostructures [6], and quantum-interference effects such as electromagnetically-induced transparency [7–10].

These approaches each achieve remarkable sensitivity; however, as we explain below, they do not necessarily satisfy the requirements for use as a scalable all-optical network element. Another approach, one that is the subject of this review, is based on the control of transverse patterns generated by nonlinear optical interactions. This pattern-based approach achieves a level of sensitivity that is comparable to other methods in addition to satisfying the requirements of scalability.

This review describes recent progress in the field of nonlinear optics that has demonstrated all-optical switches that are capable of controlling one beam of light with another. These devices exploit the inherent sensitivity of pattern-forming instabilities to weak perturbations and are based on transverse optical patterns that change orientation in the presence of a weak control beam, or *switch* beam. This article is designed as a review, but also contains relevant results from our recent work. The review is arranged as follows. The next section introduces the concepts of nonlinear pattern formation and provides context for the application of pattern-forming systems to problems in optical switching. Section 3 describes various approaches to all-optical switching, and introduces common metrics for comparing different devices. Section 4 summarizes recent experimental results using an all-optical switch based on transverse optical patterns that are formed in a counterpropagating-beam system. Section 5 presents numerical results obtained by simulating the interaction of gaussian beams counterpropagating through a medium that exhibits Kerr-like nonlinearity. In Sec. 6, we describe recent results based on simulations of a related system where beams counterpropagate in a semiconductor medium which exhibits excitonic nonlinearities. Finally, a discussion of future directions is given in Sec. 7.

2. Pattern Formation

The emergence of regular structure from natural processes has been observed throughout history. Found in nearly every field of science, patterns are one of the most recognizable signatures of a nonlinear dynamical system. The mathematical tools developed in the field of dynamics have been used successfully to describe a wide range of pattern forming systems in biology, chemistry, and computer science [11, 12].

The quantitative description of pattern formation requires a study of the system dynamics and their stability relative to perturbations. For spatially extended systems, the stability of the Fourier modes of the system are of interest. Hence, if infinitesimal perturbations applied to a specific mode grow as the system evolves, that mode can give rise to an instability. Instabilities such as this are responsible for pattern formation in systems with two or more dimensions.

The term *pattern selection* refers to the tendency of the system to exhibit patterns with a certain symmetry or orientation. Understanding the pattern selection process is of fundamental importance to understanding the patterns observed in the system. Many patterns are allowable solutions to the dynamics equations of the system, yet only a subset of the allowed patterns are typically exhibited. Patterns are selected both by constraints on the system and by the dynamics of the system. The optical patterns that are the subject of this review exhibit pattern selection by both mechanisms, although primarily via the system dynamics, in particular through external forcing [11].

Given a specific system, and thus specific allowed solutions, control of the generated patterns is limited to choosing from among these solutions. Hence, it is through controlling pattern selection that one can control the pattern generated by a system. Attempting to control the spontaneous patterns formed by nonlinear processes is not an intrinsically new idea. In fact, attempts to control many aspects of nature (i.e., weather, ocean currents, tides, and wind) are simply attempts to control the patterns that arise from nature's fundamental processes. There are, however, new applications for controllable pattern-formation, and one such application—controlling the flow of optical information—is described in the remainder of this review.

3. All-optical switching

An all-optical switch is a device that allows the control of one beam of light with another. Two fundamental properties of a switch are that the device exhibit at least two distinguishable states, and that the device input and output are distinguishable. There are many possible configurations where the switch can change the output power, direction, or state of polarization of a beam of light that is either propagating through a nonlinear medium or generated within the medium.

One simple all-optical switch that has been demonstrated in a wide variety of materials is based on the intensity-dependent refractive index of transparent nonlinear optical media. The intensity-dependent refractive index leads to a nonlinear phase shift experienced by a wave propagating through the medium. This effect allows light-by-light control if such a medium is inserted in one arm of an interferometer [13]. The output state of the interferometer could then be controlled by changing the phase shift experienced by one beam, i.e., by changing the optical path length of one arm of the interferometer. The phase shift depends on the total optical intensity incident on the

nonlinear material, so, if a strong control field is applied, and assuming the signal field is weak $I_{\rm signal} << I_c$, the nonlinear phase shift is given by

$$\phi_{\rm nl} = 2\frac{\omega}{c} n_2 I_c L, \tag{1}$$

where ω is the angular frequency, c is the speed of light in vacuum, L is the length of the medium, n_2 is the nonlinear index of refraction, and I_c is the intensity of the control field. For high-contrast switching, the control beam must be of sufficient strength to cause a significant change in the phase of the signal beam, $\phi_{\rm nl} \sim \pi$.

A second type of all-optical switch relies on the properties of a *saturable absorber*. The absorption experienced by a wave propagating through a homogeneously-broadened medium that exhibits saturable absorption depends on the intensity, and decreases for increasing intensity following the relation [13]

$$\alpha = \frac{\alpha_0}{1 + I/I_{\rm sat}}, \tag{2}$$

where α_0 is the absorption coefficient experienced by a weak field and $I_{\rm sat}$ is the saturation intensity.

In order to realize a switch based on saturable absorption, a strong control beam and a weak signal beam co-propagate through a material that exhibits saturable absorption. The control beam, in this case, must be of sufficient intensity to saturate the atomic response. Saturation of a two-level system corresponds to moving a significant amount of the atomic population from the ground state to the excited state. In order to maintain population in the excited state, one photon must be incident on each atom per excited state lifetime. Quantitatively, this condition is [14]

$$I \approx I_{\rm sat} = \frac{\hbar\omega}{\sigma\tau_{\rm sp}}, \tag{3}$$

where $\tau_{\rm sp}$ is the excited state lifetime, $\hbar\omega$ is the photon energy, and σ is the atomic cross section. Equation (3) must be modified for the case of a material undergoing optical pumping where the population is redistributed in time τ_g. Hence, to maintain saturation, one photon must be incident on each atom per τ_g, i.e., the relevant time scale is instead the ground-state lifetime τ_g. For a pair of isolated levels driven by resonant light, without collisional or Doppler broadening, the cross section has a maximum value of [13, 14]

$$\sigma_{\rm max} = \frac{3\lambda^2}{2\pi}, \tag{4}$$

where λ is the wavelength of incident light.

As an example, a cloud of cold-trapped rubidium atoms contained in a magneto-optic trap (MOT) satisfies the requirements for maximizing σ. The saturation intensity $I_{\rm sat} = 3$ mW/cm^2 for $\tau_{\rm sp} = 25$ ns and $\lambda = 780$ nm. Thus, for a beam with radius 2 mm, an optical power of 0.4 mW is required to actuate a saturation-based switch using such a Rb-MOT medium. Of course, one limitation of the saturation-based switch is that the switching beam must be weak relative to the saturation intensity. In the MOT case described here, the saturation intensity corresponds to a 2 mm diameter beam with a power of $P_{\rm sat} = 80$ μW, hence the power of the signal beam (the beam being turned on or off) must be much lower, $P_{\rm signal} << P_{\rm sat} = 80$ μW. Therefore, in the MOT example, the maximum allowed signal $P_{\rm signal} << 80$ μW is significantly weaker that the required switch beam power, which is equal to 0.4 mW.

To establish a convenient metric for comparing different all-optical switches having different geometries, we quantify the energy density of the control field in units of photons per $\lambda^2/(2\pi)$ [8]. In principle, a larger device that operates at n photons per $\lambda^2/(2\pi)$ can be scaled to have transverse dimension equal to the diffraction limit (λ^2) and operate with only n photons. The relationship between the saturation intensity and $\sigma_{\rm max}$ is such that an energy density that corresponds to approximately one photon per $\lambda^2/(2\pi)$ is sufficient to saturate a two-level transition. Of course, energy of this density must be applied for at least the lifetime of the excited state; otherwise, saturation will not occur. The assumption that saturation of the atomic transition is required for observing high-contrast all-optical switching led to the early conclusion that all-optical switches must operate with at least one photon per $\lambda^2/(2\pi)$ [15]. As this review shows, many recent all-optical switching schemes beat this limit by several orders of magnitude through various approaches. However, the metric remains useful as a tool for comparison across designs.

Sensitivity, measured in photons per $\lambda^2/(2\pi)$, is only one measure of switch performance. Depending on the design of a given all-optical switch, there are a wide range of applications each of which has additional requirements. The next section reviews two general application classes and outlines the requirements a switching device must satisfy for practical use.

3.1. Applications

Switches can be used in two classes of applications: information networks and computing systems. In each of these applications, information can be stored in either classical or quantum degrees of freedom. Hence, the requirements for a device vary depending on the intended application.

Classical, all-optical networks require switches to reliably redirect or gate a signal depending on the presence of a control field at the device input. Ideally, the switch shows large contrast between on and off output levels and can be actuated by low input powers. If the network carries quantum information, the switch must be triggered by an input field containing only a single quanta (photon). Additionally, in the quantum case, the quantum state of the transmitted signal field must be preserved.

If a switch is to be used as a logic element in a classical computing system, it must have the following characteristics: input-output isolation, cascadability, and signal level restoration [16]. Input-output isolation prohibits the

device output from having back-action on the device input. Cascadability requires that a device output have sufficient power to drive the input of at least two identical devices. Signal level restoration occurs in any device that outputs a standard signal level in response to a wide range of input levels. That is, variations in the input level do not cause variations in the output level. Switching devices that satisfy these requirements are considered scalable devices; the properties of the individual device are suitable for scaling from one device to a network of many devices.

While scalability describes important properties of a switching device, sensitivity provides one way to quantify its performance. A highly sensitive all-optical switch can be actuated by a very weak optical field. Typical metrics for quantifying sensitivity are: the input switching energy (in Joules), the input switching energy density (in photons per $\sigma = \lambda^2/2\pi$) [8, 15], and the total number of photons in the input switching pulse.

One may not expect a single device to satisfy all of the requirements for these different applications. For example, a switch operating as a logic element should output a standard level that is insensitive to input fluctuations. This may be at odds with quantum-switch operation where the device must preserve the quantum state of the signal field. An interesting question arises from these requirements: What happens when a classical switch is made sensitive enough to respond to a single photon? Reaching the level of single-photon sensitivity has been the goal of a large body of recent work that is reviewed below.

3.2. Previous Research on Low-Light-Level Switching

Two primary approaches to low-light-level switching have emerged, both of which seek to increase the strength of the nonlinear coupling between light and matter. The first method uses fields and atoms confined within and strongly coupled to a high-finesse optical cavity. The second method uses traveling waves that induce quantum interference within an optical medium and greatly enhance the effects of light on matter. These methods have been recently reviewed in Ref. [17], the following brief discussion and Table 1 summarize the key differences between various methods.

Cavity quantum-electrodynamic (CQED) systems offer very high sensitivity by decreasing the number of photons required to saturate the response of an atom that is strongly coupled to a mode of the cavity. Strongly-coupled CQED systems show a nonlinear optical response to fields corresponding to much less than a single cavity photon [4], and have also demonstrated the photon blockade effect where the arrival and absorption of one photon prevents subsequent absorption of a second photon [5].

A different technique for all-optical switching in cavities relies on creating and controlling cavity solitons in vertical cavity surface emitting lasers (VCSELs) [18]. A VCSEL can be prepared for cavity solitons by injecting a wide holding beam along the cavity axis. A narrow "write" beam superimposed on the larger holding beam induces a cavity soliton that persists typically until the original holding beam is turned off. This system naturally serves as a pixel-based optical memory, where solitons are written to and stored in the cavity field.

In contrast to cavity systems, traveling wave approaches can operate with multi-mode optical fields and also achieve few-photon sensitivity. Recent progress in traveling-wave low-light-level nonlinear optics has been made through the techniques of electro-magnetically induced transparency (EIT) [7, 10, 24–27]. As an example, Harris and Yamamoto [8] proposed a switching scheme using the strong nonlinearities that exist in specific states of four-level atoms where, in the ideal limit, a single photon at one frequency causes the absorption of light at another frequency. To achieve the lowest switching energies, the narrowest possible atomic resonances are required, which can be obtained in complex experimental environments such as trapped cold atoms [9, 10, 26–28].

Other low-light-level all-optical switching experiments have also been demonstrated recently in traveling-wave systems. By modifying the correlation between down-converted photons, Resch et al. [19] created a conditional-phase switch that operates at the single photon level. Using six-wave mixing in cold atoms, Kang et al. [20] demonstrated optical control of one field by applying another input switching field.

Another approach combines the field enhancement offered by optical cavities with the strong coupling of coherently prepared atoms. Bistability in the output of a cavity filled with an EIT medium that also shows large Kerr-type nonlinearity [29] exhibits switching. Photonic crystal nanocavities have also shown bistability switching [30]. Taking a different approach, Islam et al. [21] exploit a modulational instability in an optical fiber interferometer to gate the transmission of a strong beam by injecting a weak beam.

Many of these other systems satisfy some, but not all, of the criteria for scalability. Of the systems just discussed, CQED systems are designed to operate in a single field mode, which limits the number of input and output channels to one per polarization. Additionally, all fields are strongly coupled to the atom-cavity system so the control and signal fields must be of comparable strength. Thus a CQED switch is not cascadable. EIT systems suffer from a similar drawback in that the input and output fields are required to have the same power, making them not cascadable. Another highly sensitive system, the modulational-instability fiber interferometer, is both cascadable and exhibits signal level restoration. In several ways, the latter system is similar to pattern-based devices: it exploits the sensitivity of instabilities and uses a sensitive detector (an interferometer in their case and pattern orientation in the present case) to distinguish states of the switch.

Finally, there has been a very recent proposal that does not use cavities or traveling optical fields, but instead takes

Switch design	Reference	Switching photons	photons/σ	τ_r	Cascadable
CQED	Hood et al. [4]	1	10^{-4}	25 ns	N
CQED	Birnbaum et al. [5]	1	10^{-5}	25 ns	N
EIT	Zhang et al. [10]	20	10^{-5}	0.7 μs	N
Parametric Down Conversion	Resch et al. [19]	1	-	-	N
6-wave mixing	Kang et al. [20]	10^8	2	0.54 μs	N
MI in fiber	Islam et al. [21]	$\sim$2000	24	50 ps	Y
Plasmonic nanowire*	Chang et al. [6]	1	-	-	Y
Pattern-based switches					
VCSEL solitons	Hachair et al. [18]	24,000	140	500 ps	-
semiconductor quantum wells*	Kheradmand et al. [22]	-	-	$<$100 ns	Y
semiconductor quantum wells*	Schumacher et al. [23]	-	-	-	Y
Rubidium vapor	Dawes et al. [17]	600	10^{-3}	3 μs	Y

Table 1 Comparison of all-optical switching schemes. *Results of numerical simulation.

advantage of photon-induced surface plasmons excited in a conducting nano-wire that couple strongly to a two-level emitter placed nearby. This strong coupling enables effects that are similar to those observed in CQED. Specifically, Chang et al. [6] suggest that a system consisting of a nano-wire coupled to a dielectric waveguide can be used to create an optical transistor that is sensitive to a single photon. Photons in the dielectric waveguide are efficiently coupled to plasmons that propagate along the nanowire. A two-level emitter placed close to the nanowire has a strong effect on the plasmon transmission. The absorption of a single photon by the emitter is sufficient to change the nanowire from complete plasmon reflection to complete plasmon transmission. If implemented as proposed, a surface-plasmon transistor could operate with single-photon input levels, and gate signals containing many photons.

Many all-optical switches have been successfully demonstrated over a period spanning several decades. However, in almost every case, one or more important features is missing from the switching device. With the requirements of scalability and sensitivity in mind, this review presents recent results generated from a new approach to all-optical switching.

3.3. Switching with Transverse Optical Patterns

A new approach to all-optical switching is to exploit collective instabilities that occur when laser beams interact with a nonlinear medium [1]. One such collective instability occurs when laser beams counterpropagate through an atomic vapor. In this configuration, it is known that mirrorless parametric self-oscillation gives rise to stationary, periodic, or chaotic behavior of the intensity [31, 32] and/or polarization [33–35].

Another feature of counterpropagating beam instabilities is the formation of transverse optical patterns, i.e., the formation of spatial structure of the electromagnetic field in the plane perpendicular to the propagation direction [36, 37]. This is also true for recent experiments where a wide variety of patterns can be generated, including rings and multi-spot off-axis patterns in agreement with previous experiments [35, 36, 38].

Building an all-optical switch from transverse optical patterns combines several well-known features of nonlinear optics in a novel way. Near-resonance enhancement of the atom-photon coupling makes our system sensitive to weak optical fields. Using optical fields with a counter-propagating beam geometry allows for interactions with atoms in specific velocity groups leading to sub-Doppler nonlinear optics without requiring cold atoms. Finally, using the different orientations of a transverse pattern as distinct states of a switch allows one to maximize the sensitivity of the pattern forming instability. Instabilities, by nature, are sensitive to perturbations, so by combining instabilities with resonantly-enhanced, sub-Doppler nonlinearities, researchers in this field have created a switch with very high sensitivity.

4. Switching in warm Rb vapor

A pair of beams counterpropagating through a nonlinear optical medium give rise to patterns formed by light that is spontaneously emitted at an angle to the pump-beam axis. This section presents experimental results of pattern formation in a counterpropagating beam system where a sample of warm rubidium vapor serves as the nonlinear medium.

4.1. Experimental apparatus

A diagram of the atomic-vapor experimental setup is shown in Fig. 1 [17]. Two beams of light from a common laser source counterpropagate through warm rubidium vapor contained in a glass cell. The light source is a frequency-stabilized cw Ti:Sapphire laser, the output of

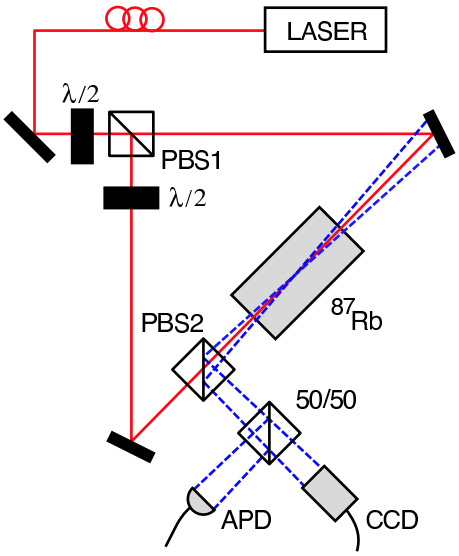

Figure 1 Experimental setup for transverse optical pattern generation. The output of a frequency-stabilized cw Ti:Sapphire laser serves as the source. A polarizing beamsplitter (PBS1) separates the forward (cw) and backward (ccw) beams within the triangular ring cavity. The backward beam is brought into horizontal polarization by a half-wave plate ($\lambda/2$). The forward and backward beams counterpropagate through a warm ^{87}Rb vapor contained in a 5-cm-long glass cell. A polarizing beam-splitter (PBS2) reflects instability-generated light in the vertical polarization which is observed by a CCD camera and avalanche photodiode (APD).

which is spatially filtered using a single-mode optical fiber with an angled entrance face and a flat-polished exit face. The beam is then collimated using a pair of convex lenses arranged as a telescope. The spot size (1/e field radius), denoted by w_0, is controlled by the configuration of the telescope, and the beam waist is located in the center of the vapor cell. The power ratio between the pump beams is controlled by a half-wave plate at the input of the first polarizing beam splitter (PBS1). We denote the beam passing through PBS1 as the forward beam and the reflected beam as the backward beam. A second half-wave plate in the backward beam path rotates the polarization such that the pump beams are linearly polarized with parallel polarizations.

The cell is fixed with length $L = 5$ cm, and a diameter of 2 cm. The cell contains a droplet of rubidium, melting point 39.3 °C, which is in equilibrium with rubidium vapor. The rubidium contained in the cell has not been isotopically enriched and thus contains the two naturally abundant isotopes: $\sim$ 72% ^{85}Rb, 28% ^{87}Rb. The cell is heated to 80 °C corresponding to an atomic number density for ^{87}Rb of 2×10^{11} atoms/cm^3. The cell has uncoated quartz windows that have fixed and opposing tilt angles of ± 11 degrees with respect to the incident laser beams to prevent possible oscillation between the windows. The cell has no paraffin coating on the interior walls that would prevent depolarization of the ground-state coherence, nor does it contain a buffer gas that would slow diffusion of atoms out of the pump laser beams. The Doppler-broadened linewidth of the transition at this temperature is $\sim$550 MHz. To prevent the occurrence of magnetically-induced instabilities and reduce Faraday rotation, a cylindrical μ-metal shield surrounds the cell and attenuates the ambient magnetic fields by a factor of $> 10^3$. In order to attenuate the static magnetic field created by the heaters coils, they are placed outside the shielding.

A polarizing beam splitter (PBS2) placed in the beam path separates light polarized orthogonally to the pump beam. This light, henceforth referred to as *output* light, is subsequently split with a 50/50 beamsplitter and then observed simultaneously using any two of the following: a CCD-camera (Marshall V-1050A), an avalanche photodiode (Hamamatsu C5460), or a photomultiplier tube (Hamamatsu H6780-20) as shown in Fig. 1.

4.2. Instability generated light

In an experimental setup similar to that described above, Dawes et al. [1, 17] observe instability generated light (output light) in the state of polarization orthogonal to that of the pump beams and with the same frequency as the pump beams. The following sections describe features of the instability as well as the conditions required for observing pattern formation. The experimental variables are the frequency of the pump light, the alignment and intensity of the pump beams, and the pump beam waist w_0.

The fixed cell length has been chosen to balance large optical depth, which increases with increasing L, and available transverse modes, which decrease with increasing L. The Fresnel number

$$\mathcal{F} = \frac{w_0^2}{\lambda L}, \tag{5}$$

quantifies the number of transverse modes supported by the geometry where λ is the wavelength [14]. Dawes et al. have observed light generated off-axis for Fresnel numbers between 1.9 and 7.8, corresponding to w_0 between 270 μm and 550 μm, respectively. The results reviewed here correspond to $w_0 = 455$ μm with $\lambda = 780$ nm, or $\mathcal{F} = 5.3$.

The other fixed parameter, the temperature, has been chosen based on optimizing the pattern-formation. Changing the temperature of the cell affects both the temperature of the atomic vapor and the atomic number density. For this work, changing the atomic number density primarily affects the optical depth of the vapor. By varying the cell temperature, and observing the amount of optical power generated by the instability, Dawes et al. found that the optimum temperature is 80° C. Fitting the absorption profile at $T = 80°$ C to a model for Rubidium absorption, they find that the maximum Doppler-broadened optical depth at this temperature is $\alpha L \simeq 55$ [17].

4.2.1. Pump-beam frequency

The power of the output light is maximized (and the threshold for the instability is lowest) when the frequency of the pump beams is set near an atomic resonance, i.e., the instability occurs near either the D_1 or D_2 transition of ^{87}Rb. The results reviewed here are for pump-beam frequencies near the D_2 transition ($^5S_{1/2} \rightarrow {}^5P_{3/2}$, 780 nm wavelength).

Figure 2 shows the power of the output light as a function of pump frequency detuning, defined as $\Delta = \nu - \nu_{F=1,F'=1}$ in cycles/s. One can observe several sub-Doppler features, where the maximum power emitted in the orthogonal polarization occurs when the laser frequency ν is tuned $\Delta = +25$ MHz. The Doppler-broadened linewidth of the transition at this temperature is ~ 550 MHz, hence, the generated light is only emitted for pump frequencies in a narrow range within the Doppler profile. For this detuning, 3.5 μW of output light is generated in the forward direction, indicating that $\sim$ 1% of the incident pump power is being converted to the orthogonal polarization. Because the detuning is small relative to the Doppler width, a significant amount of the pump light is absorbed by the medium. Although the medium is optically thick ($\alpha L \sim 55$), there is substantial bleaching with 415 μW of forward pump-beam power, which allows transmission of 50 μW of forward pump light. Of this transmitted power, 3.5 μW, or $\sim$ 7%, is converted to the orthogonal polarization [17]. In the next section, we discuss how the presence of absorption affects the instability.

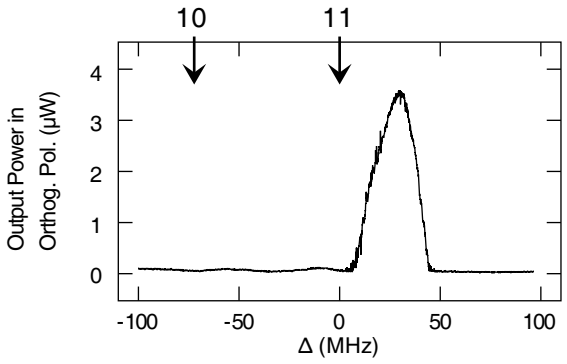

Figure 2 Instability-generated optical power as a function of pump laser frequency detuning ($\Delta = \nu - \nu_{F=1,F'=1}$). The plot shows the power generated in the forward direction and in the state of polarization orthogonal to that of the pump beams. These data correspond to a single scan through the $^5S_{1/2}(F = 1) \rightarrow {}^5P_{3/2}(F')$ transition in ^{87}Rb from low to high frequency. The bold tick marks at the top of the frame indicate the hyperfine transitions labeled by FF', where F (F') is the ground (excited) state quantum number. Pump beam power levels for this data are 415 μW (forward) and 145 μW (backward), and $w_0 = 455\,\mu$m.

The instability clearly occurs on the blue-detuned (high-frequency) side of the $^5S_{1/2}(F = 1) \rightarrow {}^5P_{3/2}(F' = 1)$ transition. This is the side of the resonance where the nonlinear refractive index has a positive value and hence self-focusing is expected to occur. This experimental observation agrees with theoretical models and can be explained using a simple argument based on weak-wave retardation [39]. The forward four-wave-mixing process can only become phase matched for off-axis beams if the nonlinear refractive index n_2 has a positive value, i.e., on the high-frequency side of an atomic resonance [13]. If n_2 is negative, the off-axis wavevectors are shortened, and thus cannot be phase-matched to the pump-beams regardless of the angle θ [13, 40].

The width of the feature shown in Fig. 2 changes with pump power such that it is narrower near threshold. This change indicates that phase matching depends on the pump power such that a wider range of frequencies are phase-matched for larger pump powers. The amount of power generated in the orthogonal polarization is also lower near threshold and increases linearly with increasing pump power as described in the following section.

4.2.2. Pump-beam intensity

The instability observed in this system has a very low threshold; the power required to induce self-oscillation is less than 1 mW, which is comparable to the results obtained from coherently-prepared atomic media [25]. A common way to measure the instability threshold for a setup with counterpropagating beams is to fix the power of one of the beams and measure the output power as a function of the power in the second pump beam [25, 34]. For a pump-beam detuning of $\Delta = +25$ MHz and with a fixed forward pump power of 415 μW, Dawes et al. find that the backward pump power threshold is $\sim$75 μW, corresponding to a total pump power of 490 μW [17].

Another way to measure the instability threshold is to determine the minimum total pump power necessary to generate output light. We find that there is an optimum ratio of forward power to backward power of $\sim$3-to-1. At this ratio, the threshold for off-axis emission is 385 μW, which is slightly lower than the threshold measured with fixed forward beam power. Dawes et al. report patterns and switching with $\sim$560 μW of total power, corresponding to 40% above threshold. Both threshold measures demonstrate that the nonlinear process that generates new light is induced by a pair of very weak fields. This indicates strong nonlinear matter-light interaction comparable with the best reported results to date for warm-vapor counterpropagating beam systems [25].

For most of the early observations of nearly-degenerate instabilities, strong pump fields were used (typically hundreds of mW) [36, 38, 41]. A considerably higher threshold was reported for the first observation of polarization instabilities in a sodium vapor [34], where a threshold of tens of mW was found when the pump fields were tuned

near an atomic resonance. More recently, Zibrov et al. [25] observed parametric self-oscillation with pump powers in the μW regime using a more involved experimental setup ("double-Λ" configuration) designed specifically to lower the instability threshold. In their experiment, atomic coherence effects increase the nonlinear coupling efficiency. They report oscillation with several mWs of total pump power. With 5 mW of forward-beam power, their instability threshold corresponds to 20 μW in the backward beam. In contrast, the results reviewed here demonstrate that spontaneous parametric oscillations are induced by μW-power counterpropagating pump-beams without the need for special coherent preparation of the medium. Furthermore, Zibrov et al. observed only on-axis emission, whereas Dawes et al. found that off-axis emission requires roughly half as much pump power as on-axis emission with our pump beam configuration. In situations where low power and high sensitivity are important, such as in all-optical switching, the lower instability threshold may make off-axis instabilities preferable.

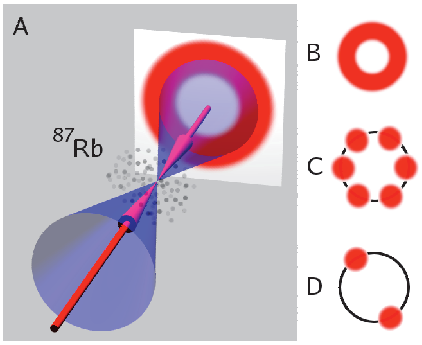

Figure 3 Light is generated along cones (blue) centered on the pump-beam axis when pump beams (red) of a sufficient intensity counterpropagate through warm rubidium vapor. A far-field detection plane shows patterns formed by the generated light. b) A ring pattern is expected for a perfectly symmetric system. c) Six spots form a hexagon, the typical pattern for pump beam powers more than 20% above threshold. d) Two spots are observed just above threshold or when the pump beams are mis-aligned. From Ref. [1]

4.2.3. Patterns

In the context of all-optical switching, pattern formation is the most notable feature of the counterpropagating beam instability described above. When the pump beams are above threshold, i.e., have total power greater than 420 μW, generated light is emitted at an angle $\theta \simeq 4$ mrad with respect to the pump beam axis, as shown in Fig. 3(a). A perfectly symmetric system is expected to generate light with intensity that is distributed evenly around the azimuthal angle, and hence would form a ring pattern in the far field. Perfect symmetry, however, is unattainable in the laboratory where imperfections in optical elements impart small perturbations on the phase and amplitude of the beams. The instability responds to such perturbations by generating patterns that are not cylindrically symmetric. For this reason, the most common patterns reported consist of two, four, or six spots in a variety of arrangements. In all cases, the spots are located along the ring projected by the cones onto the detection plane as illustrated in Fig. 3(b-d).

Most theoretical treatments consider only the case where the pump beams are strictly counterpropagating, corresponding to pump beams with equal and opposite wavevectors. In experiments, it is common to have slight mis-alignment, either intentional or accidental, between the pump beams.

With misaligned pump beams, the generated patterns change. This change is due to a change in the phase-matching conditions for the different azimuthal angles. Hence, there are different amounts of gain for different off-axis beams, and for those each beam that experiences sufficient gain for self-oscillation, a spot will be generated in the pattern. Alignment of the pump beams provides one method for pattern selection in the counterpropagating-beam system.

4.2.4. Secondary instability

In addition to the instability responsible for pattern formation, the system exhibits a secondary modulational instability (MI) that is manifested as oscillations in the intensity of the generated light. The frequency of the intensity oscillations due to this instability depends on the alignment of the pump beams. For well-aligned beams, counterpropagating along a common axis, the MI is generally suppressed as long as the pump-beam intensity is not significantly far above threshold. Figure 4 illustrates the onset of this secondary instability for the case of slightly misaligned pump beams. The threshold behavior described previously is evident here as well: the power generated in the orthogonal polarization increases linearly above 385 μW total pump power. Also visible is the saturation of the pattern-forming instability near 800 μW, where increasing the total pump power no longer increases the generated power. The height of the vertical bars indicates the peak-to-peak amplitude of oscillations due to the secondary MI. There is a notable increase in the amplitude of the MI oscillations above 560 μW total pump power (indicated in the figure), and a significant increase above 800 μW total pump power.

When the pump beams are made to counterpropagate with a small angle between their axes, observing the photodetector signal with a spectrum analyzer reveals a harmonic series with a fundamental frequency that increases for larger angular separation of the pump beam axes. The spectrum for pump beams misaligned with ~ 0.4 mrad between the beam axes has a fundamental frequency of 250 kHz [42]. The atomic vapor system operating with

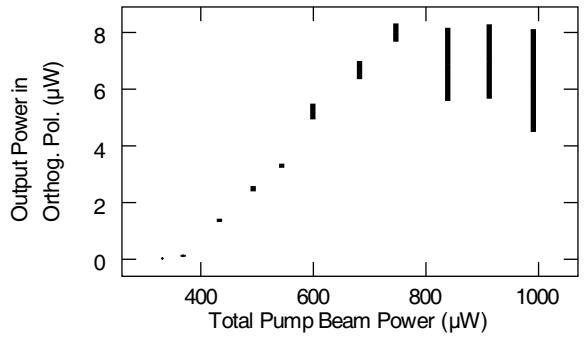

Figure 4 The peak-to-peak oscillations generated by the secondary modulational instability are indicated by the vertical bars. The output light generated in the orthogonal polarization is plotted as a function of total pump-beam power. Data are collected with fixed forward-to-backward pump-beam power ratio of 3:1, and detuning $\Delta = +25$ MHz.

this amount of pump beam misalignment exhibits sensitive switching as discussed in the next section

4.3. Switch response

To quantify the dynamic behavior of their switch, Dawes et al. inject a series of pulses by turning the switch beam on and off with the EOM [17]. Spatially filtering the output pattern enables direct measurement of the switch behavior. High-contrast switching is confirmed by simultaneously measuring two output ports. Figure 5(a) indicates the power of the injected switch beam as a function of time. The signal from the off-state detector is shown in Fig. 5(b) and is high when the switch beam is not applied and low during a switch-beam pulse. The on-state detector is shown in Fig. 5(c) and shows the opposite behavior: it is low when the switch beam is not applied and high during each switch-beam pulse. These alternating signals demonstrate switching of the power from one switch state to another with high contrast. The total power generated in the pattern is $\sim 3\,\mu$W. Each aperture selects one of the two generated spots, so the switch output power is $\sim 1.5\,\mu$W per aperture. Of course, two apertures could be used per switch state to transmit the full $\sim 3\,\mu$W output.

One notable feature of the system response is the transition from complete switching to partial switching. The first three pulses in Fig. 5 show that the on-state detector is fully illuminated and the off-state detector is dark. This indicates that the switch beam has caused complete rotation of the pattern and transferred all of the power from the off-state spots to the on-state spots. For the last seven pulses in the series, the system exhibits partial switching, where the on-state detector is partially illuminated and the off-state detector is partially darkened. This partial response indicates that the off-state spots are suppressed but not extinguished when the switch beam is applied with less than 900 pW. Similarly, the on-state spots are generated but not at full power. In this intermediate regime, from 900 pW to $<$300 pW, the response depends on the input power.

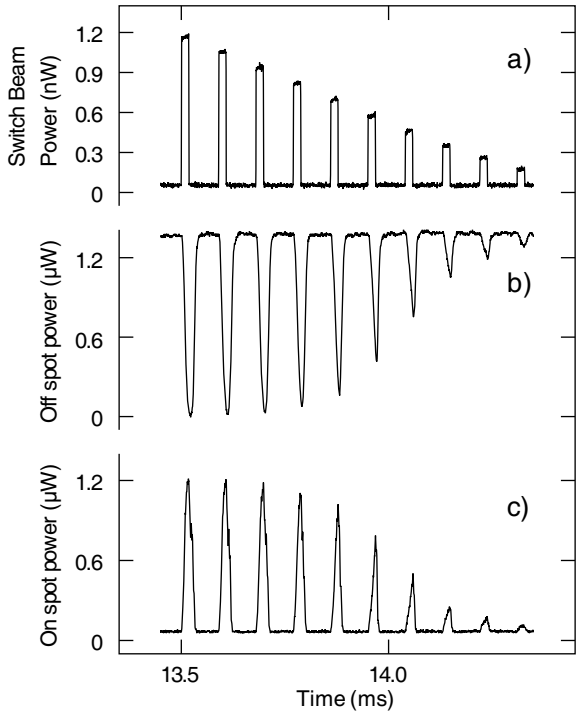

Figure 5 The switch responds to a series of ten pulses by transferring power from the *off* state spots to the *on* state spots. a) The switch beam power steadily decreases in power from 1.2 nW to 200 pW. b) The off spot is extinguished in the presence of the switch beam. c) The on spot power increases in the presence of the switch beam. The data shown are collected in a single shot that contains 22 additional ten-pulse sets with similar response. No signal averaging has been performed on the switch response data (b,c). The measured switch-beam power shown in (a) is averaged over 10 shots.

Barely visible in Fig. 5 is a the secondary modulational instability that causes small oscillations in the total output power. The modulation period of this secondary instability ($4\ \mu$s$= 1/250$ kHz) and the characteristic response time of the switch both correspond roughly to the transverse transit time of a thermal atom through the pump beams. This is a typical time scale for nonlinearities due to optical pumping.

4.3.1. Switching photon number

To quantify the sensitivity of the system, Dawes et al. measure the response time and calculate the number of photons N_p required to actuate the switch. The response time of the device τ_r is defined as the time between the initial rising edge of the electronic signal driving the EOM and the point where the on-spot signal crosses a threshold level set to roughly correspond to a signal-to-noise ratio of $\sim$3 dB.[1] Results using this threshold are shown in Fig. 6(a) and we find that the measured response time increases as the input switch beam power decreases.

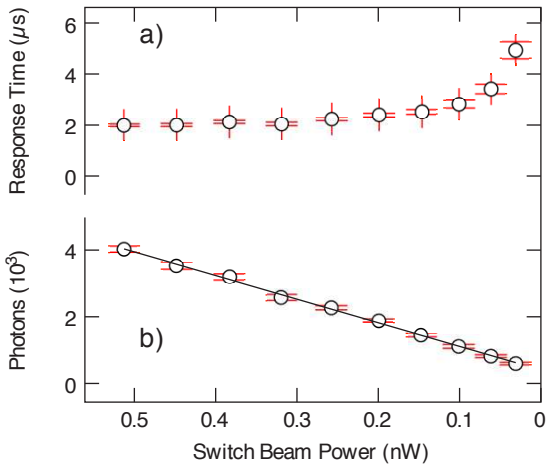

Figure 6 The response time τ_r and number of switching photons N_p as a function of input power. Data are generated from 22 sequential traces like the one shown in Fig. 5 acquired after a single trigger. The error bars indicate one standard deviation of the measured values. The solid line indicates the fit: $N_p = 7081P_s + 404$ for P_s in nW. It should be noted that the response times for the switch are on the order of a few μs, whereas the response time of the measurement system is < 35 ns.

The number of photons required to actuate the switch is given by $N_p = \tau_r P_s / E_p$ where τ_r is the response time, P_s is the switch beam power and $E_p = 2.54 \times 10^{-19}$ J is the photon energy. For ten switch-beam powers between 510 pW and 35 pW, the response time is plotted in Fig. 6(a), and the number of switching photons is plotted in Fig. 6(b). The response time is longer for weak switch-beam powers so the photon number decreases gradually as the input power decreases. The data points indicate the average of 22 data points for each of the ten switch-beam pulses, and the error bars represent one standard deviation in the response times observed for each pulse.

The implication of the linear regression shown in Fig. 6(b) is that, in the limit as $P_s \to 0$, the number of switching photons $N_p \to 400$. This would indicate that the minimum number of photons capable of actuating the switch is roughly 400. The final data point shown correspond to switching with $N_p = 600 \pm 40$, only 200 photons above this limit, and a factor of $\sim$5 lower than the first reported observation of pattern-based all-optical switching with 2,700 photons [1].[2]

4.3.2. Transistor-like response

The response shown in Fig. 5, demonstrating the saturated and linear response regimes, suggests that this device operates in a manner that is analogous to an electronic transistor. Furthermore, the two response regimes exhibited by the switch indicate that the output satisfies the conditions for signal level restoration, as discussed in Sec. 3.1.

For a device to exhibit signal level restoration, variations in the input level cannot cause variations in the output level. In every device, however, there is a narrow range of input levels, known as the intermediate region, that lead to intermediate output levels. For input levels above or below the intermediate range the output is *saturated* as a logic high or low respectively. In the case of the Rb-vapor device, this intermediate region is between 900 pW and $<$35 pW. For input levels above 900 pW, the output is high with a level set by the pump beam power.

Signal level restoration is a key property of the electronic transistor enabling large networks of electronic logic elements. This demonstration of an optical logic element that exhibits level restoration is a key step towards practical optical switches. An all-optical transistor would have applications in many data processing and communication networks in the future.

One notable limitation of the atomic-vapor switch system is the slow response time (on the order of 3 μs). A related approach, based on optical pattern formation in semiconductor systems, shows promise as a high-speed, high-bandwidth system. The details of nonlinear optical pattern formation in semiconductor systems, and a discussion of recent work, is presented in Section 6.

5. Numerical results

In order to establish the necessary ingredients for a theoretical model to describe the switching behavior observed experimentally, we develop a simple extension to a previous model of a pattern-forming counterpropagating beam system. Based on the model of Firth and Paré [44], numerical simulations performed by Chang et al. describe

[1] The SNR$\sim$3 dB criterion corresponds to the threshold where the bit-error-rate decreases below 0.05, *i.e.*, it is the point where pulses can be correctly detected with probability greater than 5% [43].

[2] The error reported in this value of N_p is a combination of statistical error in the measurement of the switch-beam power ($\sim$0.5%), and statistical variations in the response time measured for 22 sequential shots ($\sim$5%).

hexagonal pattern formation in a counterpropagating beam system [45]. We extend this prior work by simulating all-optical switching with transverse patterns. Specifically, we simulate the effect of a weak switch beam on the orientation of the hexagonal pattern generated by gaussian pump beams that counterpropagate through a Kerr-type nonlinear medium. Simulations of the time response of this system show behavior that is qualitatively similar to experimental observations. In particular, the response time increases as the switch-beam power decreases.

5.1. 3D model

The model used in these simulations is described in Ref. [44] and has been extended for our investigations to the case of two transverse dimensions. We assume scalar fields, i.e., the model does not account for the vector nature of the fields, and hence cannot describe polarization instabilities, and we do not include absorption effects. Nonetheless, this model is sufficient to describe pattern formation in counterpropagating-beam nonlinear optical systems. The forward and backward fields counterpropagating through a Kerr-like medium are described by the dimensionless equations

$$\left(\frac{\partial}{\partial z}+\frac{\partial}{\partial t}\right)F=\frac{i}{4\pi\mathcal{F}}\nabla_{\perp}^{2}F+i(|F|^{2}+2|B|^{2})F, \tag{6}$$

$$\left(-\frac{\partial}{\partial z}+\frac{\partial}{\partial t}\right)B=\frac{i}{4\pi\mathcal{F}}\nabla_{\perp}^{2}B+i(|B|^{2}+2|F|^{2})B. \tag{7}$$

Time is normalized by the transit time through the medium, $t_r = n_0 L/c$, the longitudinal dimension z is normalized by the medium length, and the transverse dimensions x, y are normalized by the beam waist w_0 where $\mathcal{F}$ is the Fresnel number, see Eq. (5). F (B) is the forward (backward) field amplitude. The nonlinear coefficient n_2 is scaled into the field amplitudes and is assumed to be positive as appropriate for the experimental conditions described in Sec. 4.1. The medium length is also scaled into the field amplitudes such that $F^2 = IL$ where I is the pump-beam intensity. One consequence of this scaling is that the product IL represents the nonlinear phase shift, in radians, experienced by an off-axis wave.

The transverse profile of the pump waves are assumed to be Gaussian such that

$$F(x,y,0,t)=F_0 e^{-(x^2+y^2)}e^{i(K_x x+K_y y)}+\xi(x,y), \tag{8}$$

$$B(x,y,L,t)=B_0 e^{-(x^2+y^2)}, \tag{9}$$

where L is the medium length, $K_{x,y}$ sets the misalignment between forward and backward wave-vectors, and ξ is a delta-correlated Gaussian random variable with $\langle\xi\rangle = 0$. The random time-independent noise source is included to simulate the effects of small spatial variations in the input beam. Typically, the peak-to-peak noise amplitude is set to $\Delta\xi = 0.01$, equivalent to 1 percent of the pump field amplitude.

Equations (6) and (7) are solved numerically using a split-step beam propagation method where linear diffraction is computed via fast Fourier transform [46]. The numerical grid of 256 by 256 transverse points and 20 longitudinal slices. The numerical grid is slightly rectangular with the x dimension 1% larger than the y dimension. This prevents the square symmetry of the grid from biasing the pattern formation process. Additionally, suitable choice of parameters and appropriate spatial filtering are used in order to avoid spurious high-K instabilities [47, 48].

5.2. Controlled pattern rotation

The primary result presented by Chang et al. is the formation of hexagonal patterns in a three-dimensional model of gaussian beams counterpropagating through a medium exhibiting Kerr nonlinearity. Their simulations are conducted with $\mathcal{F} = 63.7$ and $IL = 0.565$, where the threshold for plane-wave pattern formation predicted by Firth and Paré is $IL \simeq 0.45$. Therefore, Chang et al. simulate pattern formation for pump beams that are 25% above the minimum plane-wave threshold.

We have conducted simulations with a wide range of values of $\mathcal{F}$ between 64 and 4, where our experimental conditions correspond to $\mathcal{F} = 5.3$. Simulations in this range all exhibit hexagonal pattern formation and reproduce the results of Chang et al. In order to simulate the specific geometry of our experiment, the results reviewed here are of simulations where $\mathcal{F} = 5.3$ and $IL = 0.565$ ($\sim 25\%$ above threshold).

Images of the far field pattern generated in a typical simulation are shown in Fig. 5.2(A), where the time corresponding to each frame is indicated in units of the transit time t_r. In the initial frame of Fig. 5.2(A), the transmitted forward pump-beam is visible at the center, and the weak off-axis perturbation is visible to the right. This perturbation is used to quickly induce hexagonal pattern formation. Without the initial perturbation, hexagons are spontaneously generated after 100-150 transit times. At $t = 17$, the field that is conjugate to the perturbation, and due to forward four-wave mixing, is visible to the left of the central pump. The dark dot in the center of the first two frames is the result of numerical filtering used to remove the DC artifact introduced by computing the far-field via FFT.[3] At $t = 23$, a ring pattern has formed that is replaced by hexagons at $t = 53$. The seed beam is turned off at $t = 35$ and is not visible at $t = 53$. It is interesting to note that the ring pattern, predicted by generalizing the models of Yariv and Pepper [49] or Firth and Paré [44] to cylindrically symmetrical transverse dimensions is a transient solution that appears early ($t = 23$) in the development of

[3] This filtering is only performed on the images in order to improve the contrast, and not during the simulation itself.

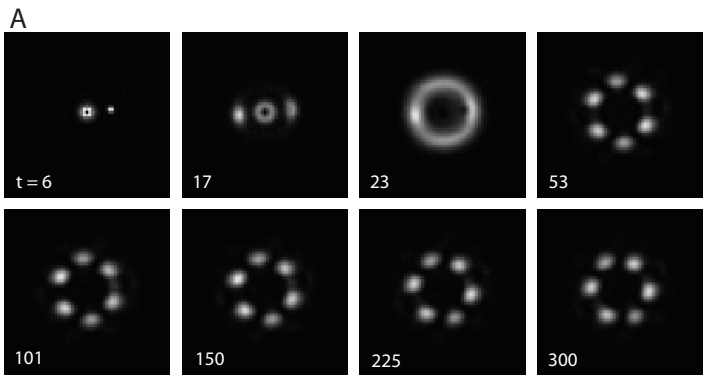

Figure 7 Numerical simulation of counterpropagating gaussian beams shows ring and hexagon pattern formation in the far field. (A) For this case, the pump beams are perfectly counter-propagating $K_x = K_y = 0$. (B) The location of the on- and off-state apertures are indicated relative to the initial hexagon pattern that forms at $t = 53$. The on-state aperture (upper square) is located opposite the applied switch beam, and the off-state aperture (lower square) transmits the spot immediately counter-clockwise from the on-state aperture.

the off-axis patterns. The ring is not a stable solution for the system in the presence of symmetry breaking, due in this case to the initial seed beam, and the ring breaks up into six spots after a short time. The second row of frames shown in Fig. 5.2(A) are collected after the application of an off-axis switch-beam, which turns on at $t = 85$, and are discussed in the next section.

5.3. Switch response

In our simulations, much like in the experiments of Dawes et al. [17], we observe that injecting a weak switch beam into the nonlinear medium after hexagons have formed causes the hexagon pattern to rotate such that a bright spot is aligned to the direction of the switch beam. This rotation is illustrated in the lower four frames of Fig. 5.2(A). The switch beam is applied at $t = 85$, and becomes visible between the two right-side spots at $t = 101$. For the frames shown, the switch beam power is $P_s = 10^{-4}P_p$, where P_p is the power of each of the counterpropagating pump beams. At $t = 150$, the counterclockwise rotation of the pattern can be observed and continues until the end of the simulation at $t = 300$ where the pattern has rotated such that the locations that were previously bright are now dark.

As in the experiments, the patterns generated in this simulation can be spatially filtered in order to define two or more output channels. Figure 5.2(B) indicates the location of the apertures used to filter the numerical results. Square apertures are used for numerical efficiency, but the results are not expected to differ if they are replaced with round apertures. The power transmitted by these apertures is calculated by summing the simulated intensity values within each aperture. For four simulation runs, each with different switch-beam power, the power transmitted through the on- and off-state aperture as a function of time t is shown in Fig. 8(a) and (b), respectively.

After the initial transients in the pattern formation, the power in the off- and on-spots stabilize within 50 transit times. At $t = 85$, the switch-beam is applied and the pattern begins to rotate, transferring power from the off-state

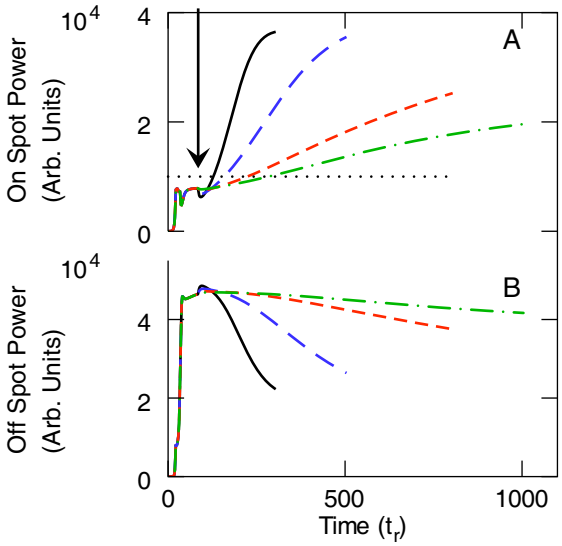

Figure 8 The power transmitted by apertures in the numerical model exhibits switching behavior that is similar to the experimental system. The response of the on- and off-state aperture transmission is shown for four levels of switch-beam power. The switch beam is turned on at $t = 85$, indicated by the arrow in (a). As the switch-beam power decreases, the simulation exhibits slower response, i.e., slower pattern rotation. The switch-beam power (in units of pump-beam power) corresponding to these four traces are 10^{-4} (solid black), 2.5×10^{-5} (large dash blue), 4×10^{-6} (small dash red), and 1×10^{-6} (dash-dot green). The horizontal dotted line indicates the threshold used to calculate response times for the simulated switch.

aperture to the on-state aperture. For $P_s = 10^{-4}P_p$, complete rotation occurs within 200 transit times. For lower switch beam power, the pattern rotates more slowly as the remaining traces show in Fig. 8. To compare the change in response time observed in the simulation to that observed experimentally, we measure the response time of the sim-

ulated switch as the time between the application of the switch beam ($t = 85$) and the threshold crossing for the on-spot. The threshold, also shown in Fig. 8, is chosen to roughly correspond to the threshold level used in the experiments.

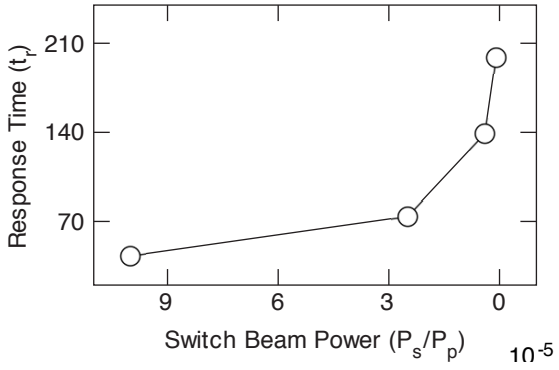

Figure 9 Simulation of the switch exhibits an increase in response time for decreasing power that is qualitatively similar to experimental observations. To facilitate comparison to Fig. 6(a), the horizontal axis has high switch-beam power to the left and low switch-beam power to the right.

The response time of the simulated switch data shown in Fig. 9 ranges from 40 transit times to 210 transit times, as shown in Fig. 9. For comparison, the transit time of the 5-cm-long vapor cell used in our experiment is 160 ps, so the simulated response times would correspond to experimental values of 6.4 ns and 33.6 ns respectively. Experiments observe response times between 2 and 4 μs in Rb vapor, so it is clear that this numerical model does not agree quantitatively with these observations. However, the simulated response time does exhibit a sharp increase in the limit of low switch-beam power, which is qualitatively similar to experimental observations. This increase in response time for weak inputs may be an indication that the switch undergoes critical slowing down [12], which would not be surprising since the orientation of the pattern exhibits multi-stability between the preferred orientations.

Another notable feature of these numerical results is that, despite the limitations of the model, the amount of switch-beam power, relative to the total pump power, required to rotate the pattern is of the same order of magnitude as what has been observed experimentally. For reference, Table 2 shows the correspondence between the normalized switch-beam power P_s/P_p used in the simulations presented above and the experimental values, based on total pump-beam power of $P_p = 560$ μW from the experiments in Ref. [17]. As an example, the third curve in Fig. 8 corresponds numerically to $P_s = 4 \times 10^{-6} P_p$. In the work of Dawes et al., this switch-beam to pump-beam power ratio would imply a switch-beam power of 1 nW and their

P_s/P_p	P_s[nW]
1×10^{-4}	26
2.5×10^{-5}	6.5
4×10^{-6}	1
1×10^{-6}	0.26

Table 2 The correspondence between P_s/P_p and P_s in nW based on 560 μW of total pump power.

switch typically operates between 1 nW and 50 pW. Therefore, the sensitivity demonstrated in experimental work is largely described by this model.

There are certainly features of the experiment that these simulations do not capture. In the first case, absorption is neglected in assuming a Kerr-type nonlinearity. One consequence of this is that misalignment of the pump beams in the simulation does not serve to reduce the number of spots generated. This is in contrast to the experiment, where misaslignment of the pump beams results in a pair of spots rather than a hexagon. This is likely due to the fact that, without simulating absorption, there is no loss experienced by the less-favored hexagonal components and, even for large pump-beam misalignment, the pattern remains a hexagon. Simulations that include misalignment of the forward pump beam exhibit hexagonal pattern formation in addition to fluctuations in the pattern orientation and a near-field pattern flow [50]. Just as for well-aligned pump beams, the switch beam also causes pattern rotation when the forward pump beam is misaligned, and the switch response time diverges near zero switch-beam power in the misaligned case as well.

Symmetry breaking may be responsible for pinning the orientation of the pattern. Including pump-beam misalignment in these simulations does appear to have this effect and is the focus of ongoing work. Refinement of the model to include absorption and saturation may also improve the agreement between experiment and simulation. Furthermore, because we have assumed a medium with an instantaneous nonlinear response, the only timescale in the Kerr model is the transit time. This leads to significantly faster switch response in the model compared to experimental observations. To quantitatively model the response time requires a more refined model of the nonlinear interaction that includes optical pumping effects and the associated time scales.

Although these initial simulations of pattern-based all-optical switch exhibits a fast response time, the experimental implementation in atomic vapor is relatively slow, and hence is a low-bandwidth system. Recent work has explored the possibility of extending these initial results by developing semiconductor systems that exhibit nonlinear optical pattern-formation. The final section describes nonlinear optics in a semiconductor system, and reviews recent results that demonstrate that such systems are potential candidates for high-bandwidth all-optical devices.

6. Semiconductor systems

The promising experimental results on pattern switching in atomic vapor (gaseous) systems have raised the question whether similar effects can be expected in solid state systems, in particular semiconductors. One obvious advantage of semiconductors over atomic systems would be the fact that they can be more easily integrated in optoelectronic communications networks. Currently, many semiconductor devices are based on III-V compounds, such as GaAs, but beyond that there is a large variety of other systems, from II-VI compounds to group-III-nitride materials to zinc oxide materials to silicon structures. Quite generally, semiconductor systems offer great flexibility in terms of epitaxial system growth (including active layers and mirrors), and, of course, they are mechanically robust.

While those application aspects suggest that semiconductors can be useful alternatives to the gaseous systems described in the previous sections, one needs to realize that the physics underlying the optical nonlinearities and the resulting optical instabilities are very different in semiconductors compared to gases. As we will show below, not all of these differences favor the semiconductor system. From a general point of view, we note that most semiconductor-based optoelectronic devices operate at frequencies close to the fundamental bandgap energy, i.e., they operate either close to an exciton (the exciton being a bound electron-hole pair) resonance or even in the band-to-band continuum. In order to achieve optical instabilities, the optical nonlinearity needs to be sufficiently large. Generally, this can be achieved by tuning the pump beams close to an optical resonance and by using sufficiently high intensities. We have seen in the previous sections that, in the atomic case, quasi resonant excitation (within the Doppler-broadened atomic spectral line) and high pump intensities (leading to significant bleaching of the line) created the optical instabilities. It is then natural to ask whether it is possible to create similar instabilities in a semiconductor. Excitation near the lowest exciton resonance and with sufficiently high intensity can create similar instabilities. However, under high excitation, an atomic resonance behaves very differently from an exciton resonance. In atoms, strong pumping can bleach the resonance and also lead to hole-burning and ac Stark shifts. In these cases, the nonlinearity can often be modeled, albeit approximately, by a single parameter n_2. This is in sharp contrast to excitons, where optical excitation creates a complex many-particle system that fundamentally changes the physics of the transition. For example, in the lowest-order nonlinear optical regime (the $\chi^{(3)}$-regime), optical excitation creates, among other things, two-exciton Coulomb correlations. Depending on the vectorial polarization state of the optical beams, these correlations may include bound two-exciton states (biexcitons). The biexciton resonance and the two-exciton continuum correlations lead to strong excitation-induced dephasing (EID), which is usually much larger than the corresponding contribution from PSF (compare Fig. 10b discussed below). In the language appropriate for semiconductors, the latter is associated with phase-space filling (PSF) [51]. The fact that in a semiconductor the optical pump beam creates carriers that lead to increased dephasing rates (EID) makes it generally more difficult to achieve optical instabilities. It therefore makes it necessary to study the origins of optical nonlinearities and optical instabilities in semiconductors in detail in order to provide a path toward pattern formation and all-optical switching. It is necessary to find parameter values and configurations in which the instability threshold intensity is kept small. For example, EID has a strong detuning dependence in the vicinity of the exciton resonance (where by detuning we mean the difference between the center frequency of the optical pump field, $\hbar\omega_p$ and the exciton resonance ε_x, $\Delta\varepsilon = \hbar\omega_p - \varepsilon_x$). The problem of EID can be controlled (or to some degree engineered) with the help of quantum confinement and cavity enhancement, as detailed below. Also, the optical nonlinearities depend critically on the intensity and vectorial polarization of the pump beam. Depending on the precise light beam and material parameters (including the system's geometry that may or may not include cavity mirrors), the nonlinearity can be dominated by PSF effects, instantaneous Hartree-Fock (HF) Coulomb effects, and time-retarded two-exciton correlations, to name the ones that will be discussed in more detail later.

6.1. Excitonic optical nonlinearities

Absorption spectra of non-excited direct-gap semiconductors exhibit discrete excitonic resonances, typically a few meV below the fundamental bandgap. Nonlinear processes involving excitons have been the subject of intensive research for several decades (for recent text book treatments and reviews see, for example [52–56]). In semiconductor amplifiers and lasers we do not have discrete excitonic resonances, but continuous spectral gain and absorption regions. In the following, we will focus solely on excitonic resonances, since they have been studied in great detail and their optical nonlinearities are by now well understood. Furthermore, because of their dominant role in optoelectronic device concepts, we will discuss semiconductor quantum-well systems, i.e., quasi-two dimensional systems. In thin GaAs quantum wells, the lowest optical transitions are dominated by heavy-hole excitons. In this case, the optical dipole selection rules are particularly simple. Both the heavy-hole valence and the conduction band are two-fold degenerate, and right circularly polarized light (denoted by "+") couples one valence band with one conduction band, whereas left-circularly polarized light (denoted by "-") couples the other two bands.

In order to discuss excitonic optical instabilities, it is advantageous to analyze the equation of motion of the excitonic interband polarization $p(t)$ separately from the Maxwell propagation equation. Similar to the instabilities discussed in Sec. 5.1, one can formulate the nonlinear equation of motion for $p(t)$ in a way that generalize the concept of phase-conjugate oscillation (PCO) [49].

Before describing the optical instabilities, we first discuss briefly the physical origin of the excitonic nonlinearities. If a pump beam with frequency close to the lowest exciton resonance creates many excitons in the system, the constituent electrons and holes interact via the Coulomb interaction, and in addition the Pauli principle yields PSF effects. We assume here that the intensity of the pump beam is not too high, so as to avoid exciton ionization and the formation of an electron-hole plasma. The effects of the Coulomb interaction are usually divided into (static) HF interactions and correlation effects. In the lowest-order (in the light field amplitude) nonlinear regime, and if the optical excitation contains both circular polarizations "+" and "-", the two-exciton correlations contain bound two-exciton states (biexcitons) as well as two-exciton scattering continua. If the optical excitation contains only one circular polarization (either "+" and "-"), the correlations contain only two-exciton continua. All two-exciton correlations can contribute to EID, as will be shown below. The equation of motion for the coherent excitonic interband polarization is [57–60]

$$\begin{aligned} i\hbar\dot{p}^{\pm} &= (\varepsilon_x - i\gamma)p^{\pm} \\ &\quad - \left[\phi^*_{1s}(0) - 2A^{\mathrm{PSF}}|p^{\pm}|^2\right] d_{cv}E^{\pm} + V^{\mathrm{HF}}|p^{\pm}|^2 p^{\pm} \\ &\quad + 2p^{\pm *}\int_{-\infty}^{\infty} \mathrm{d}\,t' \mathcal{G}^{\pm\pm}(t-t')p^{\pm}(t')p^{\pm}(t') \\ &\quad + p^{\mp *}\int_{-\infty}^{\infty} \mathrm{d}\,t' \mathcal{G}^{\pm\mp}(t-t')p^{\mp}(t')p^{\pm}(t')\,. \end{aligned} \tag{10}$$

Here, ε_x is the 1s-hh exciton energy, γ a phenomenological excitonic dephasing constant, d_{cv} the interband dipole matrix element and E the light field amplitude at the position of the QW. Both p and E depend on time and on the coordinate vector $\mathbf{r} = (x, y)$ in the plane of the QW. $A_{\mathrm{PSF}} = 4a_0^x\sqrt{2\pi}/7$ accounts for excitonic PSF, where the bulk exciton Bohr radius is denoted by $a_0^x \approx 170\,\mathring{A}$. The two-dimensional 1s exciton wavefunction $\phi_{1s}(\mathbf{r})$ is evaluated at $\mathbf{r} = 0$. $V^{\mathrm{HF}} = 2\pi(1 - 315\pi^2/4096)/a_0^{x2}E_b^x$ (with the exciton binding energy $E_b^x \approx 13\,\mathrm{meV}$) is the HF Coulomb matrix element. Unless otherwise noted, the time argument is t. The correlation kernels $\mathcal{G}$ are given by $\mathcal{G}^{++} = \mathcal{G}^{--} = \tilde{G}^{+}$ and $\mathcal{G}^{+-} = \mathcal{G}^{-+} = \tilde{G}^{+} + \tilde{G}^{-}$, with $\tilde{G}^{\pm}$ as defined in Eq. (22) of Ref. [60], including a two-exciton dephasing rate 2γ. In Eq. (10), we have neglected excitonic correlation of order 3 and higher, since such correlations are usually weak and very difficult to detect [61].

In order to illustrate the physical contents of the various nonlinear terms in Eq. (10), we Fourier transform the correlation functions from the time domain to the frequency (Ω) domain and show their frequency dependence in Figs. 10 and 11. In Fig. 10, we also include the effect of PSF. The corresponding G_{PSF} follows from the PSF term in Eq. (10) if E is expressed in terms of the first-order p [59]. In pump-probe configurations (including the instability analysis discussed in the next subsections), the real parts of the G's are proportional to the pump-induced shift of the exciton resonance, while their imaginary part is a measure of EID. Consistent with Ref. [59], we call $T^{++} = V^{HF} + 2\mathcal{G}^{++}$ and $T^{+-} = 2\mathcal{G}^{+-}$ the T-matrix in the "++" and "+-" channel, respectively. We see from Fig. 10a that, in a system in which there is only one circular polarization, HF yields a blue shift that overcompensates the correlation-induced red shift. PSF yields a shift that is positive (negative) below (above) the two-exciton continuum edge ($\hbar\Omega = 2\varepsilon(0)$). Adding the PSF to the HF contribution yields a negative slope on the HF blue shift with zero contribution at the two-exciton continuum edge. Figure 10b shows that, in the two-exciton continuum ($\hbar\Omega > 2\varepsilon(0)$), the two-exciton correlations yield strong EID, whereas the correlation-induced EID becomes negligible below the two-exciton continuum. Furthermore, PSF yields a small contribution to EID independent of frequency.

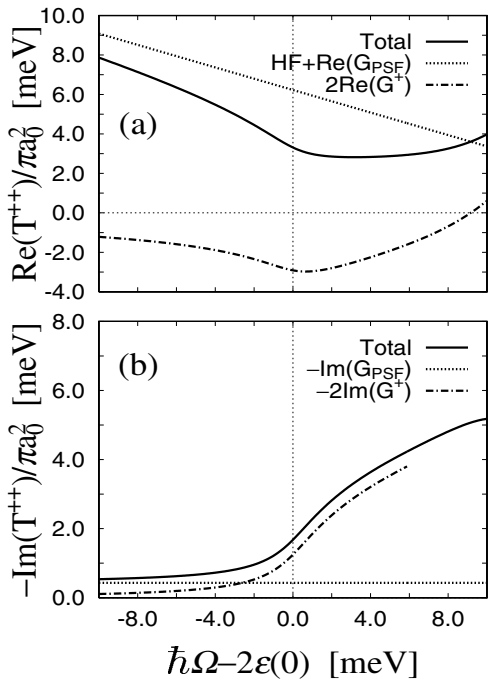

Figure 10 Exciton-exciton T-matrix in the co-circular polarization channel with $\gamma = 0.75$ meV. Here, $\varepsilon(0)$ denotes the 1s-hh exciton energy. From Ref. [59].

Figure 11a shows that, in the counter circular polarization channel, we have the biexciton resonance below the two-exciton continuum. Here, the shift has a crossover from red to blue. The biexciton resonance also yields strong EID, as can be seen in Fig. 11b. In these figures, a relatively large dephasing has been used. For smaller values of γ, the spectral region where biexcitonic EID is large becomes narrower [60].

Knowledge of the frequency dependent excitonic PSF, HF and correlation effects is crucial for the search of op-

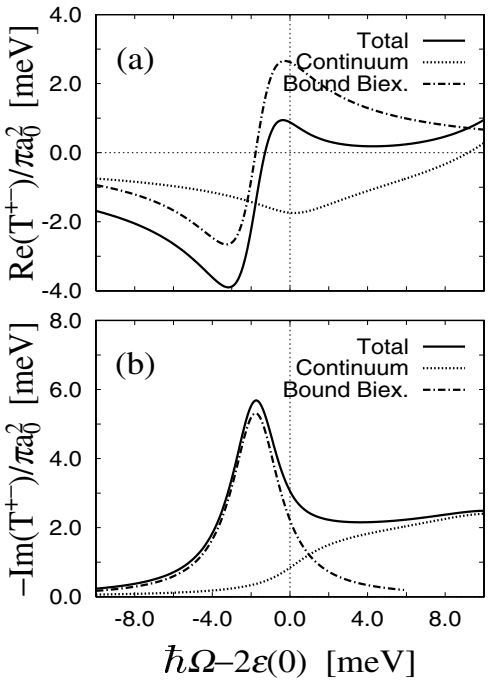

Figure 11 Same as Fig. 10, but for the counter-circular polarization channel. From Ref. [59].

tical instabilities and pattern formation. Using, as general guidelines, the criteria that a shift towards the pump frequency (which reduces the effective detuning and thus enhances the action of the pump beam) and small EID is beneficial for instabilities, we conclude from Figs. 10 and 11 that, in the co-circular channel, pumping above the two-exciton continuum yields the desired shift but unfortunately strong EID, whereas pumping below the two-exciton continuum avoids EID but unfortunately yields a HF shift of the exciton resonance away from the light frequency. We will see in Sec. 6.3 that use of a microcavity can yield a way out of this dilemma. This is because the EID increases with increasing effective mass (here the mass of the exciton). As we will discuss in more detail below, a small polariton mass in a microcavity can substantially reduce EID.

In the counter-circularly polarized channel, Fig. 11a does not give clear guidelines for possible instabilities, but one might assume that the region around the biexciton resonance may yield the desired sign of the light-induced exciton shift and small EID if the biexcitonic dephasing is sufficiently small. We will explore this possibility in the next section.

6.2. Instabilities in single quantum wells

In order to study instabilities in single quantum wells, we assume the geometry depicted in Fig. 12, with a pump beam in normal incidence and a probe beam at a small angle relative to normal incidence. The exciton polarization is restricted to the quasi-two dimensional plane of the QW. The polarization component corresponding to the background-free four-wave mixing direction, denoted in the following by the subscript f, travels in the direction $\mathbf{k}_f = 2\mathbf{k}_p - \mathbf{k}_s = -\mathbf{k}_s$, since $\mathbf{k}_p = 0$ (where all wavevectors are two-dimensional vectors). Hence, the two-dimensional spatial Fourier decomposition of the excitonic polarization, with Fourier components up to first order in the grating wavevector, yields

$$p^{\pm}(t,\mathbf{r}) = \quad p_p^{\pm}(t) + p_s^{\pm}(t)e^{i\mathbf{k}_s\mathbf{r}} + p_f^{\pm}(t)e^{-i\mathbf{k}_s\mathbf{r}}\,. \quad (11)$$

In these systems, counterpropagating beams are not needed for backward four-wave mixing and instabilities of the PCO type. One cannot distinguish between forward four-wave mixing and backward four-wave mixing.

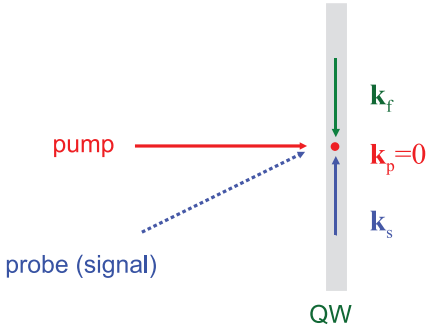

Figure 12 Geometry of the four-wave mixing process in a semiconductor quantum well (QW). The in-plane wave vectors of the interband polarization are indicated, with the pump wavevector being zero.

Because biexcitonic effects can be assumed to be critical for optical instabilities [62–65] in single quantum wells, it is advantageous to re-write Eq. (10) in a way that allows for a linear stability analysis with full inclusion of the temporal retardation effects related to biexciton formation [66]. This can be achieved by separating the continuum part and the bound biexciton part in the correlation function $\mathcal{G}^{\pm\mp} = \mathcal{G}^{\pm\mp}_{\rm cont} + \mathcal{G}^{\pm\mp}_{xx}$ and eliminating $\mathcal{G}^{\pm\mp}_{xx}$ in favor of an equation of motion for the biexciton amplitude $b(t)$, yielding new equations of motion

$$\begin{aligned} i\hbar\dot{p}^{\pm} &= (\varepsilon_x - i\gamma)p^{\pm} \\ &\quad - \left[\phi^*_{1s}(0) - 2A^{\rm PSF}|p^{\pm}|^2\right]d_{cv}E^{\pm} + V^{\rm HF}|p^{\pm}|^2p^{\pm} \\ &\quad + 2p^{\pm *}\int_{-\infty}^{\infty}\mathrm{d}\,t'\mathcal{G}^{\pm\pm}(t-t')p^{\pm}(t')p^{\pm}(t') \\ &\quad + p^{\mp *}\int_{-\infty}^{\infty}\mathrm{d}\,t'\mathcal{G}^{\pm\mp}_{\rm cont}(t-t')p^{\mp}(t')p^{\pm}(t') \\ &\quad + C^*_{xx}p^{\pm *}b(t)\,, \end{aligned} \quad (12)$$

with

$$i\hbar\dot{b} = (\varepsilon_{xx} - 2i\gamma)b + \frac{1}{2}C_{xx}p^{+}p^{-}\,, \qquad (13)$$

where C_{xx} is a function of the exciton-exciton interaction and the biexciton wavefunction, and is taken to be $0.54E_b^x a_0^x$ in the following. The propagation of the optical field $E^{\pm}$ across the QW is described with a transfer-matrix method that accounts for radiative corrections and that assumes the QW to be infinitely thin (see, for example, Eq. (A5) of Ref. [59]). It is important to note that, in a single quantum well, the excitonic polarizations are sources for light fields via radiative decay, but there is no feedback of the radiative decay on the incoming light fields. Hence, the dynamics of the system can be described solely with the equation for the excitonic polarizations. The situation will be different in the microcavity (Sec. 6.3), where the strong interaction between the excitonic polarization and the cavity mode require a full description of the system dynamics including the equations for p and E.

Using the Fourier decomposition (Eq. (11)) of Eqs. (12) and (13), it is straighforward to derive the linear set of equations of motion for $p_s^{\pm}$ and $p_f^{\pm}$ (fully given in Ref. [67]) and the nonlinear equation for the pump-induced interband polarization $p_p^{\pm}$, which is independent of $p_{s,f}^{\pm}$. The equations for $p_{s,f}^{\pm}$ contain self-wave mixing (SWM) terms, $i\dot{p}_{s,f} \sim p_{s,f}p_p^{*}E_p$ and $i\dot{p}_{s,f} \sim p_{s,f}p_p^{*}p_p$, and cross-wave mixing (XWM) terms, $i\dot{p}_{s,f} \sim p_{f,s}^{*}p_pE_p$ and $i\dot{p}_{s,f} \sim p_{f,s}^{*}p_pp_p$. The XWM terms are necessary for instabilities and possible pattern formation.

To analyze the possibility of optical instabilities, we perform a linear stability analysis (LSA). The LSA is done without an incoming probe field and for a monochromatic cw pump field $E_p^{\pm}(t) = \tilde{E}_p^{\pm}\mathrm{e}^{-i\omega_p t}$ and pump polarization $p_p^{\pm}(t) = \tilde{p}_p^{\pm}\mathrm{e}^{-i\omega_p t}$, with $\dot{\tilde{p}}_p^{\pm} = \dot{\tilde{E}}_p^{\pm} = 0$ (ω_p is the pump frequency). We evaluate the memory integrals using the Markov approximation [$p_{s,f}(t') \approx p_{s,f}(t)\mathrm{e}^{i\omega_p(t-t')}$] for the two-exciton continuum in the correlation kernels $\mathcal{G}^{\pm\pm}$, $\mathcal{G}^{\pm\mp}$. The term driving the bound biexciton amplitudes $b_{s,f}(t)$ is proportional to $p_p^{\mp}p_{s,f}^{\pm} + p_p^{\pm}p_{s,f}^{\mp}$. With the ansatz $p_{s,f}(t) = \tilde{p}_{s,f}(t)\mathrm{e}^{-i\omega_p t}$ and $b_{s,f}(t) = \tilde{b}_{s,f}(t)\mathrm{e}^{-i2\omega_p t}$, the probe and FWM dynamics take the form

$$\frac{\mathrm{d}}{\mathrm{d}t}\tilde{\mathbf{p}}(t) = M\,\tilde{\mathbf{p}}(t), \qquad (14)$$

with $\tilde{\mathbf{p}}(t) = \left[\tilde{p}_s^{+}(t), \tilde{p}_f^{+*}(t), \tilde{p}_s^{-}(t), \tilde{p}_f^{-*}(t), \tilde{b}_s(t), \tilde{b}_f^{*}(t)\right]^T$. The system is unstable if at least one of the eigenvalues λ_i of M fulfills $\mathrm{Re}\{\lambda_i\} > 0$.

Since atomic nonlinearities are clearly very successful in terms of allowing instabilities, it is instructive to first evaluate Eq. (14) for the semiconductor quantum well keeping only the atomic nonlinearities (PSF). For this case, an analytical evaluation using first-order (in the pump field amplitude) pump polarizations has been discussed in Ref. [68]. It was found that instability driven only by

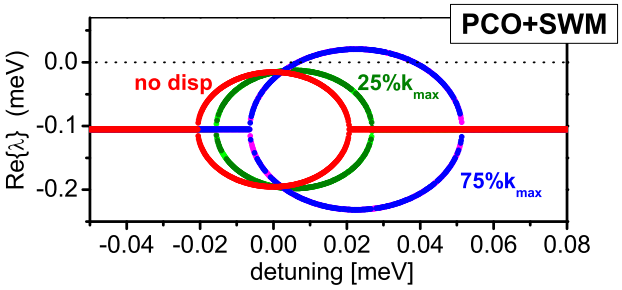

Figure 13 Linear stability analysis for a linearly polarized pump for steady-state total coherent exciton density $n_x^{\mathrm{total}} = 1.7 \times 10^{11}\mathrm{cm}^{-2}$. Shown are the real parts of the eigenvalues λ_i of the matrix M vs. pump detuning. The dotted line in panel (a) separates the stable ($\mathrm{Re}\{\lambda\} < 0$) from the unstable ($\mathrm{Re}\{\lambda\} > 0$) regime. From Ref. [68].

PSF cannot be expected. However, a generalization of the model, in which spatial dispersion of the exciton frequency is taken into account (i.e., ε_x entering the pump equation is different from that entering the signal and FWM equations) allows, at least in principle, for instabilities. This is shown in Fig. 13. We show the case of no-dispersion as well as two different in-plane wavevectors of the signal. Here, k_{max} is the maximum in-plane vector for the given frequency. Clearly, we find a region of positive eigenvalues (i.e., instabilities) for the case of $k_s = 0.75k_{\mathrm{max}}$, which indicates that spatial dispersion is indeed beneficial of the PSF-driven instability.

We stress that Fig. 13 is only a case study, meant to illustrate how PSF could in principle yield near-resonance instabilities in semiconductor quantum wells. However, PSF can only yield instabilities at positive detuning, at which correlation processes yield large EID. In the calculation leading to the result of Fig. 13, we had to use a very high density in order to obtain instability; a density where EID would clearly be very large. It is therefore necessary to study the complete system, including PSF, HF, continuum correlations and biexcitonic correlations. Solving for this case Eq. (14), we find the instabilities depend sensitively on the vectorial polarization of the pump beam. While, in this case, for circularly polarized pump beams, we find no instabilities, linearly polarized (say "X" polarized) pump beams do yield instabilities, as shown in Fig. 14. We find three different unstable regions ($\mathrm{Re}\{\lambda_i\} > 0$) caused by the biexcitonic ($+-$) XWM terms. The labels XX and XY denote the vectorial polarizations of the pump (always X) and the unstable modes or probe fluctuations (either X or Y). We see that a pump beam tuned into the two-photon resonance with the biexciton allows for a polarization instability (the unstable probe is Y polarized), whereas in the spectral region just below and above the biexciton resonance we have polarization-preserving instabilities. The XY instability and the XX instability below the biexciton are single-color instabilities (the imaginary

parts of the eigenvalues are degenerate in the instability region), whereas the XX instability above the biexciton is a two color instability. In the latter, the imaginary parts of the "unstable" eigenvalues are split, which means that we have two modes with the same growth rates but different frequencies.

While the single quantum well instabilities discussed so far could possibly be used for pattern formation, it needs to be noted that these instabilities are found to be relatively fragile. They can be expected only if the dephasing rate is very small, such as that reported in [69]. In the next subsection, we turn our focus on a less fragile instability in a different semiconductor system.

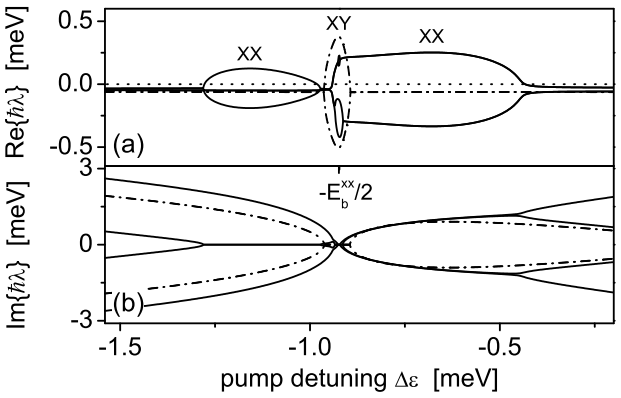

Figure 14 Linear stability analysis for a linearly polarized pump for steady-state total coherent exciton density $n_x^{\text{total}} = 1.6 \times 10^{10}\text{cm}^{-2}$. Shown are the real parts (a) and imaginary parts (b) of the eigenvalues λ_i of the matrix M for negative pump detuning. Eigenvalues are represented by solid lines for the co-linear (XX) and by dashed-dotted lines for the cross-linear (XY) polarization configuration. From Ref. [67].

6.3. Pattern switching in semiconductor microcavities

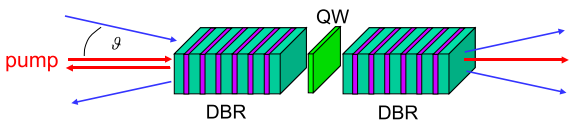

Figure 15 Sketch of a planar semiconductor quantum well (QW) microcavity, with distributed Bragg reflector (DBR) mirrors and normal-incidence pump beam.

In the following, we consider planar semiconductor microcavities, which consist of a semiconductor quantum well and two mirrors (Fig. 15). In high quality cavities, the exciton-photon coupling is strong enough so that the eigenmodes of the system become cavity polaritons [70]. The in-plane dispersion of these polaritons is shown in Fig. 16 along with the dispersions of the uncoupled excitons and photons. The parabolic dispersion of the uncoupled excitons is not visible in this figures because of the small wavevector region shown. It is apparent from the figure that the effective mass of the lower polariton branch (LPB) is much smaller than that of the uncoupled exciton. As mentioned above, small mass is related to small EID [71, 72], and the smallness of EID at the LPB has been a major factor for their usefulness in providing optical instabilities.

In the past decade, the parametric amplification of polaritons (a process usually related to optical instability) has been the subject of intense experimental and theoretical research; see, e.g., Refs. [73–78] or the reviews given in Refs. [79–81]. In a typical pump-probe setup in a co-circular polarization configuration (with the pump coming in at an angle ϑ, unlike the case shown in Fig. 15), the amplification of a weak probe pulse at normal incidence has mainly been attributed to four-wave mixing (FWM) processes mediated by the repulsive Coulomb interaction of the exciton constituent of the polaritons excited on the lower polariton branch (LPB) [72, 75, 76, 78]. For a specific pump in-plane momentum (defining the so-called "magic angle"), energy and momentum conservation is best fulfilled for the FWM processes and thus a pronounced angular dependence of this amplification is observed [73, 75]. Because, in the strong coupling regime, the LPB is spectrally well below the two-exciton scattering continuum, the influence of excitonic correlations in the scattering processes of polaritons on the LPB is strongly suppressed (compared to the situation in a single quantum well without the strong coupling to a confined photon cavity mode, as discussed in the previous subsection). However, even for co-circular pump-probe excitation, these correlations must be considered for a complete understanding of the experimental results [72, 77, 82].

In the following, we review the recent work [23, 83, 84] on optical instability and switching analogous to the atomic case (Sec. 4). We concentrate on the dynamics in one spin subsystem (say spin up) by choosing circularly polarized excitation. We neglect a possible longitudinal-transverse (TE-TM) cavity-mode splitting [85]. As a further simplification, we use the optical dipole selection rules and matrix elements appropriate in quasi-normal incidence (a complete vectorial formulation of the theory with selection rules for arbitrary angles can be found, for example, in [86]). We apply a spatial decomposition of cavity field and exciton polarization into Fourier components $E_{\mathbf{k}}$ and $p_{\mathbf{k}}$, respectively, with in-plane momentum $\mathbf{k}$ [72]. The nonlinear set of coupled equations of motion for

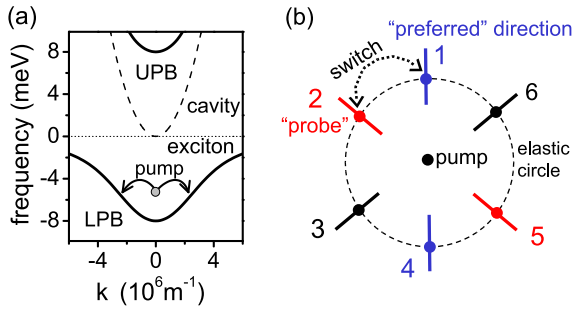

Figure 16 (a) Sketch of the linear cavity polariton dispersion. The bare cavity and exciton dispersions are shown, together with the lower (LPB) and upper (UPB) polariton branches of the coupled cavity-mode exciton system. The fundamental pairwise off-axis scattering of pump polaritons is also indicated. (b) Sketch of the hexagonal switching geometry in the transverse plane. The elastic circle is defined by the pump frequency and the dispersion of the LPB. The basic switching action triggered by the probe is indicated. The radial bars indicate the variation in the magnitude of off-axis momenta $\mathbf{k}$ as included in the nonlinear polariton dynamics. From Ref. [23].

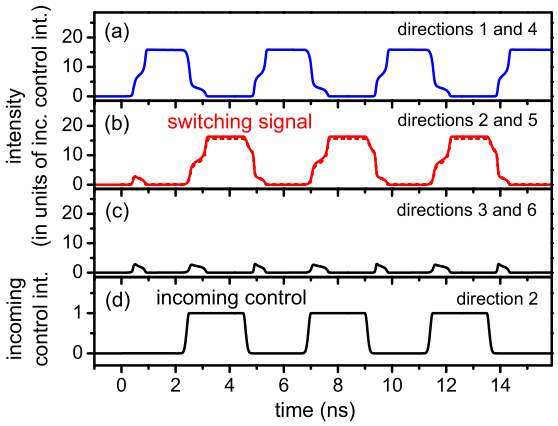

Figure 17 (a)-(c) Switching in the output signals in a reflection geometry (the signals with out-of-plane momentum opposing the incident pump's are plotted). The intensities per direction are normalized to the incoming control intensity. The switching signal in (b) is about 15 times stronger than the incoming control in (d) that is triggering this signal (note the different scales on the vertical axes in panels (a)-(c) and (d)). In panel (b), direction 2 is shown as the solid line and direction 5 as the dashed line. Similar switching is observed in a transmission geometry (not shown). From Ref. [23].

$E_{\mathbf{k}}$ and $p_{\mathbf{k}}$ reads

$$i\hbar\dot{E}_{\mathbf{k}} = \hbar\omega^c_{\mathbf{k}}E_{\mathbf{k}} - \Omega_{\mathbf{k}}p_{\mathbf{k}} + i\hbar t_c E^{\text{eff}}_{\mathbf{k},\text{inc}}\,, \tag{15}$$

$$i\hbar\dot{p}_{\mathbf{k}} = (\varepsilon^x_{\mathbf{k}} - i\gamma)p_{\mathbf{k}} - \Omega_{\mathbf{k}}E_{\mathbf{k}} + \sum_{\mathbf{q}\mathbf{k}'\mathbf{k}''}\big(2\tilde{A}\Omega_{\mathbf{k}''}p^*_{\mathbf{q}}p_{\mathbf{k}'}E_{\mathbf{k}''} + V_{\text{HF}}p^*_{\mathbf{q}}p_{\mathbf{k}'}p_{\mathbf{k}''}\big)\delta_{\mathbf{q},\mathbf{k}'+\mathbf{k}''-\mathbf{k}}\,. \tag{16}$$

The cavity-field in Eq. (15) is treated in quasi-mode approximation [87]. The effective incoming field $E^{\text{eff}}_{\mathbf{k},\text{inc}}$ driving the field $E_{\mathbf{k}}$ in the cavity mode is obtained from a simple transfer-matrix formalism that includes the radiative width ($\Gamma = \omega\hbar^2 t_c^2/(\epsilon_0 c n_{\text{b}})$, with the background refractive index n_{b}, the vacuum velocity of light c and dielectric constant ϵ_0) of the cavity mode and yields transmitted and reflected field components: $E^{\text{eff}}_{\mathbf{k},\text{inc}} = E_{\mathbf{k},\text{trans}} = E_{\mathbf{k},\text{inc}} - E_{\mathbf{k},\text{refl}}$ with $E_{\mathbf{k},\text{refl}} = -(\hbar t_c/2n_{\text{b}}c\varepsilon_0)\dot{E}_{\mathbf{k}}$. The cavity-to-outside coupling constant t_c is chosen such that $\Gamma \approx 0.4\,\text{meV}$ for $\hbar\omega = 1.5\,\text{eV}$. We include excitonic PSF and HF exciton-exciton Coulomb interaction in the nonlinear exciton dynamics in Eq. (16); two-exciton correlations are neglected in this study and are expected to give merely quantitative changes because the pump is, in what follows, tuned far (several meV) below the bare exciton resonance [71, 72] (cf. Fig. 16(a)). Inclusion of two-exciton Coulomb correlations in our calculations would basically lead to renormalization of V_{HF} in Eq. (16) and give rise to a small additional excitation-induced dephasing [71, 72]. The bare exciton and cavity in-plane dispersions are denoted by $\varepsilon^x_{\mathbf{k}}$ (with $\varepsilon^x_0 = 1.497\,\text{eV}$) and $\omega^c_{\mathbf{k}}$, with $\hbar\omega^c_{\mathbf{k}} = \varepsilon^x_0/\cos\vartheta$ and $\sin\vartheta = |\mathbf{k}|c/(\omega n_{\text{b}})$. The dephasing is $\gamma = 0.4\,\text{meV}$, $\Omega_{\mathbf{k}} = 8\,\text{meV}$ is the vacuum Rabi splitting, and $\tilde{A} = A_{\text{PSF}}/\phi^*_{1s}(0)$. A spatial anisotropy in the system can be modeled, e.g., by including an anisotropic cavity dispersion $\omega^c_{\mathbf{k}}$.

In Fig. 17, we show results where we have numerically integrated the nonlinear coupled Eqs. (15) and (16) for quasi steady-state pump excitation in normal incidence. The pump frequency is tuned $5\,\text{meV}$ below the bare exciton resonance. The pump (not shown) reaches its peak intensity $I_{\text{pump}} \approx 19.5\,\text{kW cm}^{-2}$ shortly after $0\,\text{ps}$ and is then kept constant. We impose a slight anisotropy in the cavity dispersion by shifting $\omega^c_{\mathbf{k}}$ to lower energies by $0.075\,\text{meV}$ in directions 1 and 4. Above a certain pump threshold intensity, phase-matched pairwise scattering of pump-induced polaritons, driven mainly by the HF term in Eq. (16), leads to spontaneous (fluctuation-triggered) off-axis signal formation (similar to [88, 89]). Initially, signals in all the considered off-axis directions start to grow simultaneously. However, as these signals grow over time, the anisotropy (symmetry breaking) fixes the spontaneous off-axis pattern at directions 1 and 4. This can be seen in Fig. 17(a)-(c) for times less than $2\,\text{ns}$. After $2\,\text{ns}$, we apply a weak probe ($I_{\text{probe}} \approx 0.1\,\text{W cm}^{-2}$) with the same frequency as the pump frequency in direction 2 (Fig. 17(d)). Now, the strong off-axis emission switches to directions 2 and 5 and vanishes in the "preferred" directions 1 and 4. Note that the switching signal in directions 2 and 5 is about 15 times stronger than the probe pulse itself (i.e., part of the pump is redirected from normal incidence to the directions 2 and 5). In other words, the gain in direction 2 is $\approx 11.7\,\text{dB}$. When switching off the weak probe

at $\approx 5\,\mathrm{ns}$, the strong off-axis emission switches back to the preferred directions 1 and 4. The switching can then be repeated as shown in the figure. On/off switching times in our study are $\approx 1\,\mathrm{ns}$ (corresponding to switching brought about by ≈ 13 photons if a beam waist of $2\,\mu\mathrm{m}$ diameter is assumed). Even though no systematic study into the lower limit of the switching times has been undertaken, the results imply that the bandwidth limitation (due to slow switching times) encountered in the atomic system may be significantly improved in semiconductor microcavities.

Since the pump excitation is off-resonant, a relatively strong pump is required to reach the instability threshold. In an experimental setup, unintended off-axis scattering of pump light could reduce the contrast ratio between "on" and "off" states and thus the performance of the switch. However, this practical issue might be alleviated using another existing microcavity design [90] where resonant pump excitation could be used. We have estimated that a reduction of the threshold intensity by two orders of magnitude could be expected [23].

A related study of all optical pattern switching has been given in Ref. [22]. There, a comprehensive numerical analysis of pattern formation and switching in semiconductor microcavities is presented. It has been found that patterns can be controlled with beams that have 100 times smaller intensities than the intensity of the pattern, with switching times comparable to the ones shown in Fig. 17. The nonlinearity used in [22] is restricted to PSF due to the presence of incoherent carriers, and the evaluation focuses on the positive detuning case. As discussed above, at positive detuning strong EID from correlations may be expected to hinder instability, although further investigations of EID from incoherent carriers are needed to verify this hypothesis. At any rate, the investigation in [22] supports our belief that semiconductor microcavities may be the most promising semiconductor system for future demonstrations of transverse optical pattern switching at low light levels. Experiments on stimulated polariton scattering in microcavities have shown an impressive trend towards higher operational temperatures [77, 90].

In addition to microcavities, other systems may also be candidates for instabilities and switching. For example, instabilities in the co-circular polarization channel can be expected in Bragg-spaced quantum wells [91], which are a specific realization of one-dimensional resonant photonic bandgap structures), because, in these systems, a suppression of EID as a consequence of the strong coupling between the quantum wells and the light field (similar to the case of semiconductor microcavities discussed above) is beneficial for optical instabilities.

We end the discussion of semiconductor systems by noting that, for all these systems, a substantial amount of further research is needed to experimentally verify the predicted optical switching phenomena and, once that is achieved, to make their performance characteristics compatible with the requirements of real devices.

7. Future directions

The initial results demonstrating optical patterns as a mechanism for all-optical switching have led to further research in both atomic vapor and semiconductor systems. There are many potential directions for future research. One immediate step forward is to extend the present numerical model described in Sec. 5 to allow for pump-beam misalignment. This work is presently underway and demonstrates that the symmetry breaking introduced in this way does contribute to the overall sensitivity of the switch. Additionally, improved quantitative agreement with the experimental results from the vapor system may be obtained by using an improved numerical model that takes into account the optical-pumping nonlinearity.

Experimental verification of the switching phenomena in semiconductor systems is required to confirm the current predictions. Furthermore, such devices must then be optimized for specific applications. As this review suggests, pattern-based all-optical switches can be implemented in a variety of systems. Some, such as atomic vapor, may be ideal for ultra-low-light applications, while others, such as semiconductor systems, may be ideal for high-bandwidth applications.

Acknowledgements We thank the DARPA Defense Sciences Office Slow Light project. We thank Alex Gaeta for providing examples of numerical models of counterpropagating beam systems. AMCD and DJG wish to thank the Army Research Office for provided support through grant W911NF-05-1-0228, RB, NHK and SS thank JSOP for additional support, and ALS would like to thank ONR. SS gratefully acknowledges support from the Deutsche Forschungsgemeinschaft (DFG) through grant SCHU 1980/3-1.

References

[1] A. M. C. Dawes, L. Illing, S. M. Clark, and D. J. Gauthier, Science **308**, 672 (2005).
[2] R. K. Cavin and V. V. Zhirnov, Solid-State Electronics **50**, 520 (2006).
[3] L. M. Duan, M. D. Lukin, J. I. Cirac, and P. Zoller, Nature **414**, 413 (2001).
[4] C. J. Hood, M. S. Chapman, T. W. Lynn, and H. J. Kimble, Phys. Rev. Lett. **80**, 4157 (1998).
[5] K. Birnbaum, A. Boca, R. Miller, A. Boozer, T. Northup, and H. Kimble, Nature **436**, 87 (2005).
[6] D. Chang, A. Sørensen, E. Demler, and M. Lukin, Nature Physics **3**, 807 (2007).
[7] S. E. Harris, Phys. Today **50**, 36 (1997).
[8] S. E. Harris and Y. Yamamoto, Phys. Rev. Lett. **81**, 3611 (1998).
[9] S. E. Harris and L. V. Hau, Phys. Rev. Lett. **82**, 4611 (1999).
[10] J. Zhang, G. Hernandez, and Y. Zhu, Opt. Lett. **32**, 1317 (2007).

[11] M. C. Cross and P. C. Hohenberg, Rev. Mod. Phys. **65**, 851 (1993).
[12] S. H. Strogatz, Nonlinear Dynamics and Chaos: With Applications to Physics, Biology, Chemistry and Engineering (Perseus Books Group, 2001).
[13] R. W. Boyd, Nonlinear Optics, 2nd edition (Academic Press, 2002).
[14] A. E. Siegman, Lasers (University Science Books, 1986).
[15] R. W. Keyes, Science **168**, 796 (1970).
[16] R. W. Keyes, J. Phys.: Condens. Matter **18**, S703 (2006).
[17] A. M. C. Dawes, L. Illing, J. A. Greenberg, and D. J. Gauther, Phys. Rev. A **77**, 013833 (2008).
[18] X. Hachair, L. Furfaro, J. Javaloyes, M. Giudici, S. Balle, J. Tredicce, G. Tissoni, L. A. Lugiato, M. Brambilla, and T. Maggipinto, Phys. Rev. A **72**, 013815 (2005).
[19] K. J. Resch, J. S. Lundeen, and A. M. Steinberg, Phys. Rev. Lett. **89**, 037904 (2002).
[20] H. Kang, G. Hernandez, and Y. Zhu, Phys. Rev. Lett. **93**, 073601 (2004).
[21] M. Islam, S. Dijaili, and J. Gordon, Opt. Lett. **13**, 518 (1988).
[22] R. Kheradmand, M. Sahrai, H. Tajalli, G. Tissoni, and L. A. Lugiato, Eur. Phys. J. D **47**, 107 (2008).
[23] S. Schumacher, N. H. Kwong, R. Binder, and A. L. Smirl, Low intensity directional switching of light in semiconductor microcavities, 10.1002/pssr.200802200, 2008.
[24] H. Schmidt and A. Imamoglu, Opt. Lett. **21**, 1936 (1996).
[25] A. S. Zibrov, M. D. Lukin, and M. O. Scully, Phys. Rev. Lett. **83**, 4049 (1999).
[26] D. A. Braje, V. Balić, G. Y. Yin, and S. E. Harris, Phys. Rev. A **68**, 041801 (2003).
[27] Y. F. Chen, Z. H. Tsai, Y. C. Liu, and I. A. Yu, Opt. Lett. **30**, 3207 (2005).
[28] M. Yan, E. G. Rickey, and Y. Zhu, Phys. Rev. A **64**, 041801 (2001).
[29] H. Wang, D. Goorskey, and M. Xiao, Phys. Rev. A **65**, 051802 (2002).
[30] T. Tanabe, M. Notomi, S. Mitsugi, A. Shinya, and E. Kuramochi, Opt. Lett. **30**, 2575 (2005).
[31] Y. Silberberg and I. Bar-Joseph, J. Opt. Soc. Am. B **1**, 662 (1984).
[32] G. Khitrova, J. F. Valley, and H. M. Gibbs, Phys. Rev. Lett. **60**, 1126 (1988).
[33] A. L. Gaeta, R. W. Boyd, J. R. Ackerhalt, and P. W. Milonni, Phys. Rev. Lett. **58**, 2432 (1987).
[34] D. J. Gauthier, M. S. Malcuit, and R. W. Boyd, Phys. Rev. Lett. **61**, 1827 (1988).
[35] D. J. Gauthier, M. S. Malcuit, A. L. Gaeta, and R. W. Boyd, Phys. Rev. Lett. **64**, 1721 (1990).
[36] A. Petrossian, M. Pinard, A. Maître, J. Y. Courtois, and G. Grynberg, Europhys. Lett. **18**, 689 (1992).
[37] L. A. Lugiato, Chaos, Solitons, & Fractals **4**, 1251 (1994).
[38] G. Grynberg, E. Le Bihan, P. Verklerk, P. Simoneau, J. R. R. Leite, D. Bloch, S. Le Boiteux, and M. Ducloy, Opt. Commun. **67**, 363 (1988).
[39] R. Y. Chiao, P. L. Kelley, and E. Garmire, Phys. Rev. Lett. **17**, 1158 (1966).
[40] G. Grynberg, Opt. Commun. **66**, 321 (1988).
[41] A. Maître, A. Petrossian, A. Blouin, M. Pinard, and G. Grynberg, Opt. Commun. **116**, 153 (1995).
[42] A. Dawes, Using Transverse Optical Patterns for Ultra-Low-Light All-Optical Switching, unpublished, Duke University, April 2008.
[43] P. Kish, The effect of network cabling on bit error rate performance, Tech. rep., NORDX/CDT, April 2000.
[44] W. J. Firth and C. Paré, Opt. Lett. **13**, 1096 (1988).
[45] R. Chang, W. J. Firth, R. Indik, J. V. Moloney, and E. M. Wright, Opt. Commun. **88**, 167 (1992).
[46] J. Fleck, J. Morris, and M. Feit, Appl. Phys. A **10**, 129 (1976).
[47] W. J. Firth, C. Penman, and C. Paré, Opt. Commun. **75**, 136 (1990).
[48] C. Penman, W. J. Firth, and C. Paré, J. Mod. Opt. **37**, 719 (1990).
[49] A. Yariv and D. M. Pepper, Opt. Lett. **1**, 16 (1977).
[50] T. Honda, Opt. Lett. **20**, 851 (1995).
[51] N. H. Kwong, I. Rumyantsev, R. Binder, and A. L. Smirl, Phys. Rev. B **72**, 235312 (2005).
[52] H. Haug and A. P. Jauho, Quantum Kinetics in Transport and Optics of Semiconductors (Springer, Berlin, 1996).
[53] D. Chemla and J. Shah, Nature **411**, 549 (2001).
[54] W. Schäfer and M. Wegener, Semiconductor Optics and Transport Phenomena (Springer, Berlin, 2002).
[55] H. Haug and S. W. Koch, Quantum Theory of the Optical and Electronic Properties of Semiconductors, 4th edition (World Scientific, Singapore, 2004).
[56] T. Meier, P. Thomas, and S. Koch, Coherent Semiconductor Optics (Springer, New York, 2006).
[57] V. M. Axt and A. Stahl, Z. Phys. B **93**, 195 (1994).
[58] T. Östreich, K. Schönhammer, and L. J. Sham, Phys. Rev. Lett. **74**, 4698 (1995).
[59] N. H. Kwong, R. Takayama, I. Rumyantsev, M. Kuwata-Gonokami, and R. Binder, Phys. Rev. B **64**, 045316 (2001).
[60] R. Takayama, N. H. Kwong, I. Rumyantsev, M. Kuwata-Gonokami, and R. Binder, Eur. Phys. J. B **25**, 445 (2002).
[61] V. M. Axt, T. Kuhn, B. Haase, U. Neukirch, and J. Gutowski, Phys. Rev. Lett. **93**, 127402 (2004).
[62] N. Peyghambarian, H. M. Gibbs, M. C. Rushford, and D. A. Weinberger, Phys. Rev. Lett. **51**, 1692 (1983).
[63] M. Inoue, Phys. Rev. B **33**, 1317 (1986).
[64] S. W. Koch and H. Haug, Phys. Rev. Lett. **46**, 450 (1981).
[65] D. T. Nguyen, Phys. Lett. A **193**, 462 (1994).
[66] C. Sieh, T. Meier, F. Jahnke, A. Knorr, S. W. Koch,

P. Brick, M. Hübner, C. Ell, J. Prineas, G. Khitrova, and H. M. Gibbs, Phys. Rev. Lett. **82**, 3112 (1999).
[67] S. Schumacher, N. H. Kwong, and R. Binder, Europhys. Lett. **81**, 27003 (2008).
[68] S. Schumacher, N. H. Kwong, R. Binder, and A. L. Smirl, submitted, Physica Status Solidi (b) (2008).
[69] W. Langbein, T. Meier, S. W. Koch, and J. V. Hvam, J. Opt. Soc. Am. B **18**, 1318 (2001).
[70] G. Khitrova, H. M. Gibbs, F. Jahnke, M. Kira, and S. W. Koch, Rev. Mod. Phys. **71**, 1591 (1999).
[71] N. H. Kwong, R. Takayama, I. Rumyantsev, M. Kuwata-Gonokami, and R. Binder, Phys. Rev. Lett. **87**, 027402 (2001).
[72] S. Savasta, O. Di Stefano, and R. Girlanda, Phys. Rev. Lett. **90**, 096403 (2003).
[73] P. G. Savvidis, J. J. Baumberg, R. M. Stevenson, M. S. Skolnick, D. M. Whittaker, and J. S. Roberts, Phys. Rev. Lett. **84**, 1547 (2000).
[74] R. Huang, F. Tassone, and Y. Yamamoto, Phys. Rev. B **61**, R7854 (2000).
[75] C. Ciuti, P. Schwendimann, B. Deveaud, and A. Quattropani, Phys. Rev. B **62**, R4825 (2000).
[76] R. M. Stevenson, V. N. Astratov, M. S. Skolnick, D. M. Whittaker, M. Emam-Ismail, A. I. Tartakovskii, P. G. Savvidis, J. J. Baumberg, and J. S. Roberts, Phys. Rev. Lett. **85**, 3680 (2000).
[77] M. Saba, C. Ciuti, J. Bloch, V. Thierry-Mieg, R. Andre, Le Si Dang, S. Kundermann, A. Mura, G. Bongiovanni, J. L. Staehli, and B. Deveaud, Nature **414**, 731 (2001).
[78] D. M. Whittaker, Phys. Rev. B **63**, 193305 (2001).
[79] C. Ciuti, P. Schwendimann, and A. Quattropani, Semicond. Sci. Technol. **18**, 279 (2003).
[80] J. J. Baumberg and P. G. Lagoudakis, Phys. Stat. Sol. (b) **242**, 2210 (2005).
[81] J. Keeling, F. M. Marchetti, M. H. Szymanska, and P. B. Littlewood, Semicond. Sci. Technol. **22**, R1 (2007).
[82] S. Savasta, O. Di Stefano, and R. Girlanda, Semicond. Sci. Technol. **18**, S294 (2003).
[83] S. Schumacher, N. H. Kwong, R. Binder, and A. L. Smirl, arXiv.org:cond-mat/0712.2060v1 (2007).
[84] S. Schumacher, N. H. Kwong, R. Binder, and A. L. Smirl, CLEO/QELS Conference Proceedings p. No. QMC4 (2008).
[85] V. Savona, F. Tassone, C. Piermarocchi, A. Quattropani, and P. Schwendimann, Phys. Rev. B **53**, 13051 (1996).
[86] S. Schumacher, N. H. Kwong, and R. Binder, Phys. Rev. B **76**, 245324 (2007).
[87] S. Savasta and R. Girlanda, Phys. Rev. Lett. **77**, 4736 (1996).
[88] M. Romanelli, C. Leyder, J. Ph. Karr, E. Giacobino, and A. Bramati, Phys. Rev. Lett. **98**, 106401 (2007).
[89] A. Verger, I. Carusotto, and C. Ciuti, Phys. Rev. B **76**, 115324 (2007).
[90] C. Diederichs, J. Tignon, G. Dasbach, C. Ciuti, A. Lemaitre, J. Bloch, P. Roussignol, and D. Delalande, Nature **440**, 904 (2006).
[91] S. Schumacher, N. H. Kwong, and R. Binder, Appl. Phys. Lett. **92**, 131109 (2008).